Enhancing air–sea CO_2 exchange and modulating seawater carbonate–pH dynamics: the role of wave effect mechanisms in the POP2–waves coupled model

Yung-Yao Lan[1,2], Huang-Hsiung Hsu[1], Wei-Liang Lee[*1] and Simon Chou[1]

[1]Research Center for Environmental Changes, Academia Sinica, Taipei 11529, Taiwan

[2]National Land Resources Conservation Center, National Chung Hsing University, Taichung 40227, Taiwan

Correspondence to: Wei-Liang Lee (leelupin@gate.sinica.edu.tw)

Abstract

In this study, a wave module is online-coupled into the Parallel Ocean Program version 2 (POP2) within the CESM1.2.2 framework (hereafter POP2–waves). Unlike empirical data analyses of observation-based products and offline-forced ocean models that treat wave-induced gas transfer velocity and the air–sea difference in partial pressure of CO_2 ($dpCO_2$) as decoupled variables, the online-coupled POP2–waves model captures their interactive, $dpCO_2$-driven negative feedbacks. This setup enables wave properties to dynamically modulate gas transfer velocity and physical mixing through sequential processes. POP2–waves is evaluated alongside a control simulation (B–CTL) against the National Oceanic and Atmospheric Administration (NOAA) CarbonTracker (CT2022) inversion product. The spatial air–sea CO_2 flux in POP2–waves shows closer structural agreement with the NOAA CT2022 than the control B–CTL. Specifically, bubble-mediated transfer accounts for up to 41.3% of the total flux, consistent with the ~40% contribution reported in recent research. POP2–waves enhances regional oceanic CO_2 uptake and outgassing by 11.8% and 41.6%, respectively, yielding a 1.8% increase in the global net ocean CO_2 sink compared to the B–CTL simulation. Globally, air–sea $dpCO_2$ and pH exhibit the strongest positive and negative regression coefficients with the air–sea CO_2 flux. Regionally, the gas transfer velocity shows a positive (negative) regression coefficient within oceanic CO_2 outgassing (uptake) regions, whereas SST displays the opposite trend.

1. Introduction

The exchange of CO_2 between the air and sea is a crucial component of the global carbon cycle, carrying significant implications for Earth's climate (Bange et al., 2024; Friedlingstein et al., 2022; McKinley et al., 2020; Müller et al., 2023; Shutler et al., 2019). Traditionally, this air–sea exchange is characterized using the bulk formula (e.g., Wanninkhof, 1992, 2014; McKinley et al., 2020; Dong et al., 2022; Fay et al., 2021; Zhou et al., 2023; Heimdal et al., 2024):

$$F_{CO_2} = k_{w,660} \cdot k_0 \cdot (pCO_2^w - pCO_2^a) \cdot (1 - ice) \quad (1)$$

where the air–sea CO_2 flux (F_{CO_2}, mol m^{-2} yr^{-1}) is determined by the gas transfer velocity expressed relative to a Schmidt number of 660 ($k_{w,660}$, cm hr^{-1}), the difference in partial pressure of CO_2 ($dpCO_2$, μatm) between the seawater and atmosphere (indicated by superscripts " *w* " and " *a* ", respectively), and the solubility constant (k_0; mol m^{-3} atm^{-1}), which varies with salinity and temperature (Weiss, 1974). Note that an appropriate scaling factor (8.76×10^{-5}) is implicitly required to convert the dimensions of $k_{w,660}$ and $dpCO_2$ into the final flux unit (mol m^{-2} yr^{-1}). The sign of air–sea CO_2 flux is determined by $dpCO_2$, where a positive air–sea CO_2 flux indicating ocean outgassing to the atmosphere. Additionally,, the calculated fluxes are weighted by the ice-free fraction (1 – *ice*), where '*ice*' represents the sea ice fraction. The estimation of bulk air–sea CO_2 fluxes using the gas transfer velocity is typically based on the Wanninkhof (1992) formulation:

$$k_{w,660} = 0.31 \langle U_{10}^2 \rangle (Sc/660)^{-0.5} \quad (2)$$

where $\langle U_{10}^2 \rangle$ represents the squared neutral mean wind speed at 10 m above the surface (m s^{-1}), and *Sc* denotes the Schmidt number. The flux estimate error can reach as high as 34% due to model limitations and uncertainties surrounding bulk parameters. (Signorini and McClain, 2009). Furthermore, substantial uncertainties persist in air–sea

CO_2 flux estimates, primarily stemming from an incomplete understanding of the spatiotemporal variability in the governing mechanisms (Shutler et al., 2019).

Some studies have highlighted that estimating air–sea CO_2 fluxes involves complexities well beyond neutral wind speed and solubility factors. Monahan and Spillane (1984) previously regarded whitecaps as "low impedance vents", that effectively "shorten" the water-side transfer resistance. Without wave breaking, air–sea CO_2 exchange occurs via mass transport, which under non-turbulent conditions is governed by molecular diffusion, wave breaking then acts as a transitional process from laminar to turbulent flow (Deike, 2022). Furthermore, bubbles provide additional surface area for gas transfer; as they rise through the aqueous mass boundary layer and burst at the sea surface, they significantly enhance near-surface turbulence (Soloviev and Lukas, 2010; Bell et al., 2017; Deike and Melville, 2018; Krall et al., 2019; Czerski et al., 2022). Gutiérrez-Loza et al. (2022) pointed out that during high and intermediate wind speeds (>6–8 m s^{-1}), enhanced air–sea CO_2 exchange is primarily driven by wave-breaking dynamics and bubble mediation, which occur alongside the generation of sea spray droplets that contribute to atmospheric cloud condensation nucleation. Conversely, under low wind conditions (<6 m s^{-1}), water-side convection becomes the dominant control mechanism. Beyond these calm periods, the critical role of breaking waves and bubble injection mechanisms in facilitating CO_2 transfer has been widely corroborated (e.g., Andreas et al., 2016; Brumer et al., 2017; Blomquist et al., 2017; Reichl and Deike, 2020; Li et al., 2023; Zhou et al., 2023; Rustogi et al., 2025). Specifically, Deike and Melville (2018) demonstrated that the bubble-mediated contribution to CO_2 transfer exceeds 40% at a neutral 10-meter wind speed (U_{10}) ≥ 10 m s^{-1}, becomes dominant at U_{10} ≥ 15 m s^{-1} and reaches 60% at 20 m s^{-1}.

Monitoring sea surface CO_2 is crucial for understanding Earth system dynamics, as climate change has begun to impact the ocean's carbon uptake capacity (Behncke et

al., 2024). However, air–sea CO_2 fluxes estimates derived from products based on the partial pressure of CO_2 (pCO_2) often suffer from significant uncertainties, primarily because they rely on empirical parameterizations of the gas transfer velocity (e.g., Williams et al., 2017; Gray et al., 2018; Coggins et al., 2023; Behncke et al., 2024; Fay et al., 2024; Yang et al., 2024). To resolve this issue and independently constrain $k_{w,660}$, direct flux measurements using the eddy covariance (EC) method are widely utilized as a benchmark reference (Dong et al., 2021). By directly acquiring the turbulent flux F_{CO_2} via the EC method and pairing it with simultaneous measurements of $dpCO_2$, researchers can inversely calculate the gas transfer velocity ($k_{w,660} = F_{CO_2} / (k_0 \times dpCO_2)$). This approach provides a direct observational constraint to evaluate and calibrate these observation-based products under complex marine conditions. However, obtaining reliable direct fluxes from shipborne EC setups presents its own instrumental challenges. Marine EC systems are generally conducted using either open- or closed-path infrared gas analyzers. A closed-path analyzer (e.g., LI-7000, LI-COR) operates with an enclosed measurement chamber (Sutton et al., 2014, 2021; Bakker et al., 2016; Sabine et al., 2020; Akhand et al., 2021; Wu and Qi, 2023), whereas open-path analyzers (e.g., LI-7500, LI-COR) measure infrared absorption directly in ambient air (Edson et al., 2011; Tokoro et al., 2014; Bell et al., 2017; Dong et al., 2021; Van Dam et al., 2021). While both configurations are inherently susceptible to H_2O cross-sensitivity, each system possesses distinct advantages and systematic limitations (Honkanen et al., 2018). Evaluating and constraining global Earth system models (ESMs) with direct, long-term observations of air–sea CO_2 flux remains challenging due to the severe scarcity of continuous field measurements. Consequently, alternative validation datasets are typically derived by upscaling sparse shipbased pCO_2 observations combined using statistical interpolation, machine learning, atmospheric inversion, and climatological averaging to construct long-term, gridded flux products.

Although several recent studies have estimated the air–sea CO_2 flux using Eq. (1), current parameterizations in oceanic and atmospheric models still rely exclusively on neutral wind speed (Long et al., 2013; Moore et al., 2013; Couldrey et al., 2016; Jin et al., 2017; Lovenduski et al., 2019; Ziehn et al., 2020; Chikamoto and DiNezio, 2021). Similarly, surface ocean observation-based products typically calculate those flux using standard parameterizations (Wanninkhof et al., 1992, 2014; Fay et al., 2021). Crucially, the persistent uptake of anthropogenic CO_2 is lowering seawater pH and altering carbonate system in nonlinear ways, which further reducing the oceans' capacity to absorb additional CO_2 (Moore et al., 2013). The mechanisms of breaking waves and bubble injection in facilitating the total gas transfer velocity have been investigated primarily through empirical data analyses of observation-based products (e.g., Andreas et al., 2016; Blomquist et al., 2017; Reichl and Deike, 2020; Zhou et al., 2023). Rustogi et al. (2025) employed a fully coupled ocean–biogeochemistry modeling system based on the MOM6 ocean circulation model and the COBALTv2 biogeochemical module. Utilizing this framework, they simulated ocean dynamics, temperature, and carbon cycling processes—including dissolved inorganic carbon (DIC) and pCO_2—while explicitly accounting for wave effects on air–sea CO_2 exchange. Furthermore, they identified a nonlinear pCO_2 feedback mechanism within the coupled ocean–carbon system that regulates air–sea CO_2 flux. However, their configuration relies on ocean and biogeochemical modules that are strictly forced by offline atmospheric reanalysis and wave model outputs. This decoupled or single-directional forcing approach faces limitations in capturing high-frequency, transient air–sea interactions (e.g., rapid wind shifts or wave breaking dynamics) that significantly modulate gas exchange. In contrast, our study introduces an online coupling framework that integrates wave effects directly into the flux simulation interface at each model time step. This online approach provides a key value-add by enabling real-time, interactive feedback between wave dynamics

and the seawater carbonate system, thereby resolving the non-linear high-frequency physical controls on the air–sea CO_2 flux that are often overlooked in offline-forced systems.

In this study, we investigate how breaking waves and bubble injection mechanisms influence air–sea CO_2 flux and ocean's buffering capacity. Specifically, we examine the biogeochemical responses driven by these physical mechanisms within the seawater carbonate–pH system. To achieve this, we utilize the Parallel Ocean Program version 2 (POP2; Smith et al., 2010) of the Community Earth System Model version 1.2.2 (CESM1.2.2; Hurrell et al., 2013) online coupled with waves module (Mellor et al., 2008) of the Princeton Ocean Model (POM; Blumberg and Mellor, 1987). The coupled model is referred to as the POP2–waves model.

The structure of this paper is organized as follows. Section 2 introduces the model, data, methodology, and experiments employed in this study, and defines twelve key regions of high air–sea CO_2 flux variability identified by NOAA CT2022 to validate the model simulation. Section 3 evaluates the performance of the POP2–waves coupled model in simulating air–sea CO_2 flux and its interaction with the carbonate–pH system over the Western Pacific (WP; 160–180°E, 35–40°N) and the Equatorial Pacific (EP; 230–250°E, 0–5°S) regions. Section 4 compares the carbonate–pH dynamics of POP2–waves and B–CTL, examine the primary drivers of air–sea CO_2 exchange, and evaluate the uncertainties arising from the absence of $dpCO_2$-driven negative feedback. Finally, Section 5 presents the conclusions.

2. Data, model experiments, and methodology

2.1 Description of the model framework and experiments

In this study, we investigated the role of waves and bubble mechanisms in modulating ocean biogeochemistry response by comparing the control simulation (B–

CTL) with the coupled POP2–waves model within the CESM1.2.2 framework (Fig. 1). The CESM simulation was conducted using a fully coupled component set over a 30-year period, with well-mixed greenhouse gases (CO_2, CH_4, N_2O, etc.), ozone, and aerosols fixed to year-2000 values (the B_2000_CAM5 compset). The framework features a horizontal resolution of 1.9° × 2.5° in the Community Atmosphere Model 5.3 (CAM5.3) and a nominal 1° horizontal resolution with 60 vertical layers in POP2, the Community Land Model version 4 (CLM4), the prognostic Los Alamos Sea Ice Model (CICE), and the coupler (CPL) (Hurrell et al., 2013). POP2 is forced by CAM5.3 through CPL via four primary fields: (1) momentum fluxes (zonal and meridional wind stress and friction velocity), (2) heat fluxes (net shortwave radiation, sensible heat flux, longwave radiation, and heat flux from snow/ice melt), (3) freshwater fluxes (precipitation, evaporation, river runoff, and ice melt), and (4) surface winds (10 m zonal and meridional wind speeds). Furthermore, POP2 interacts with the Marine Biogeochemistry (MARBL; Long et al., 2021) module to regulate carbonate chemistry and air–sea CO_2 fluxes. This interaction is mediated via ocean dynamics (currents and sea surface height), K-profile vertical mixing, and tracer transport, with wave-induced processes providing additional physical constraints. Within MARBL, variations in DIC and nutrients (NO_3, PO_4, and Fe) are primarily controlled by biological processes: photosynthesis consumes DIC and nutrients, whereas respiration and remineralization return organic carbon to the DIC pool. Together with the wave module, these biogeochemical and physical processes jointly regulate the carbon cycle.

The control simulation (B–CTL), which served as the baseline for air–sea CO_2 flux and seawater acidification , utilized Eq. (1) with the gas transfer velocity according to Wanninkhof (1992) (Eq. 2). Both the B–CTL and POP2–waves experiments were integrated under a present-day scenario (starting from the year 2000) to estimate air–sea CO_2 flux pH variations. This experimental design allowed us to isolate the impact

of wave effects on carbonate chemistry and directly compare our results with the NOAA CarbonTracker CT2022 product (Jacobson et al., 2023). For the POP2–waves experiment, the waves module (Mellor et al., 2008) from the POM model was online coupled into POP2. This configuration incorporated bubble-mediated gas transfer—computed from a mechanistic model for air bubble entrainment at the breaking-wave scale (Deike and Melville, 2018)—integrated with the POP2 marine biogeochemistry module.

Specifically, POP2–waves experiment adopts the advanced parameterization framework expanded by Reichl and Deike (2020), and Deike (2022). In this framework, both the non-bubble and bubble-mediated gas transfer velocity are explicitly resolved as a function of the ocean surface friction velocity, (u^*, m s^{-1}) and significant wave height, (H_s, m). This parameterization effectively captures the main wave effect, as well as solubility and diffusivity. To standardize the formulation for CO_2, the total gas transfer velocity is expressed relative to a Schmidt number of 660. Following Deike and Melville (2018), it is calculated as the sum of the non-bubble ($k_{\mathrm{wNB},660}$) and bubble ($k_{\mathrm{wB},660}$) components:

$$K_{\mathrm{w},660} = K_{\mathrm{wNB},660} + K_{\mathrm{wB},660} = A_{NB} u^* \left(\frac{Sc}{660}\right)^{-1/2} + \frac{A_B}{K_0 R T_0} (u^*)^{5/3} (g H_s)^{2/3} \left(\frac{Sc}{660}\right)^{-1/2} \quad (3)$$

where A_{NB} is an empirical, nondimensional coefficient given as 1.55×10^{-4}, A_B is a dimensional fitting coefficient (1.2×10^{-5} s^2 m^{-2}), R is the ideal gas constant (0.082 L atm mol^{-1} K^{-1}), T_0 is the sea surface temperature, SST (K), and g is gravitational acceleration (9.806 m s^{-1}). Section 3.3 examines the contribution ratios of the non-bubble and bubble components in simulating the air–sea CO_2 flux.

The marine carbonic acid system is a nonlinear, coupled system governed by CO_2 dissolution equilibrium, ($CO_{2(aq)} + H_2O \overset{K_H}{\leftrightarrow} H_2CO_{3(aq)}$), where the Henry's constant (K_H) for CO_2 in water at 25°C is approximately 3.4 x 10^{-2} (m atm^{-1}), two-step

dissociation reactions, and the conservation of the total dissolved inorganic carbon (DIC) and total alkalinity (TA), ultimately determining pH and the distribution of carbonate species. The H_2CO_3 has two hydrogen ions and dissociates in two steps:

$$H_2CO_3 \overset{K_{a1}}{\longleftrightarrow} H^+ + HCO_3^- \qquad K_{a1} = 4.4 \times 10^{-7} \tag{4}$$

$$HCO_3^- \overset{K_{a2}}{\longleftrightarrow} H^+ + CO_3^{2-} \qquad K_{a2} = 4.7 \times 10^{-11} \tag{5}$$

The DIC can be expressed as

$$\begin{aligned} DIC &= [H_2CO_3] + [HCO_3^-] + [CO_3^{2-}] \\ &= K_H pCO_2^w + \frac{K_{a1} K_H pCO_2^w}{[H^+]} + \frac{K_{a1} K_{a2} K_H pCO_2^w}{[H^+]^2} \\ &= K_H pCO_2^w \left(1 + \frac{K_{a1}}{[H^+]} + \frac{K_{a1} K_{a2}}{[H^+]^2}\right) \\ &= K_H pCO_2^w ([H^+]^2 + K_{a1} [H^+] + K_{a1} K_{a2}) / [H^+]^2 \end{aligned} \tag{6}$$

The marine carbonate system describes the distribution of DIC among its chemical species in seawater and is jointly governed by TA and pH. From Eq. (6), if the oceanic pCO_2^w and pH are known, the DIC can be determined, conversely, pCO_2^w can be inferred from DIC. TA is defined as the sum of the proton-neutralizing capacities of all weak acid anions in seawater (Dickson, 1981) and can be expressed as:

$TA = [HCO_3^-] + 2[CO_3^{2-}] + [B(OH)_4^-] + [OH^-] + [HPO_4^{2-}] + 2[PO_4^{3-}] + [SiO(OH)_3] + [NH_3] + [HS^-] - [H^+] - [H_3PO_4]$. In the POP2–waves framework, TA, pH and biogeochemistry are also used to calculate pCO_2^w.

When TA increases, seawater becomes more alkaline, leading to a higher CO_3^{2-} concentration and enhanced buffering of hydrogen ions. Consequently, $[H^+]$ decreases, causing pH to rise and boosting the ocean's capacity to absorb CO_2. Conversely, when TA decreases, the buffering capacity weakens, $[H^+]$ increases, pH drops, rendering the ocean more acidic with a reduced ability to uptake CO_2.

2.2 Coupling POP2–waves Methodology

Except for the ocean component, all other components adhere strictly to the CESM 1.2.2 framework. The wave module is forced by variables exchanged through the coupler, the POP2, and a dedicated input initialization file. Specifically, in addition to the baseline component interactions in CESM1.2.2, the framework passes the zonal and meridional 10-m winds, along with surface friction velocity (u^*, accounting for both open-ocean and t sea-ice fractions) from the CPL to evaluate the wave properties and the associated gas transfer velocity. To drive the wave module calculations, key physical variables from POP2; this involves interpolating the depth-variable currents from the POP2 z-coordinates (60 levels of zonal and meridional horizontal velocities) onto the POM (waves) sigma-coordinates (21 vertical levels). This vertical mapping is r equired to compute both the depth-dependent wave radiation equation and the specified spectrum. Additionally, spatial grid configurations across the the x, y, and z domains and timestep configurations are exchanged. The wave module further integrates external variables (F1–F4), which represent the spectrally averaged components of wave radiation stress incorporated into the momentum equation.

Following Mellor et al. (2008), the significant wave height (H_s) utilized in the wave radiation equation represents the total wave energy integrated over the full spectrum, which inherently encompasses both locally wind-generated seas and remotely generated swells. During the simulation of wave energy and propagation, improper handling of parallel boundary formulations within the domain decomposition can induce artificial wave energy accumulation at the subdomain interfaces. To resolve this, this study mirrors the parallel computing infrastructure of the POP2 Message Passing Interface (MPI) protocol. Key wave-module prognostic variables—including the zonal and meridional 10-m winds, wave radiation stress, subsurface momentum, and wave radiation and energy densities—are explicitly integrated across processor

subdomains to establish a robust, scalable online coupling framework.

2.3 Model Validation

We evaluate the simulated spatial patterns of the air–sea CO_2 flux from both the uncoupled control simulation (B–CTL) and the coupled POP2–waves model against estimates from the NOAA CarbonTracker data assimilation system (CT2022; Jacobson et al., 2023). Unlike our forward, ocean-centric modeling frameworks, CT2022 constraints the system from an atmospheric perspective, top-down inferring net surface CO_2 fluxes by assimilating observed atmospheric CO_2 mole fractions. Consequently, this product captures the integrated signature of both anthropogenic emissions and natural carbon cycle variability to providing continuous global flux estimates spanning January 2000 through December 2020.

Following the inversion framework established by Jacobson et al. (2007), NOAA CT2022 partitions the global ocean into 30 distinct basins to capture large-scale circulation and biogeochemical dynamics. This basin-based approach groups regions characterized coherence in physical processes—such as major currents systems, upwelling zones, and boundary mixing layers—as well as shared biogeochemical behaviors, including air–sea CO_2 exchange rates and biological productivity. Moreover, because numerous observational datasets and ocean carbon products are resolved at regional scales, a basin-scale aggregation ensures greater methodological consistency. We evaluate the seasonal variability and mean state of global air–sea CO_2 fluxes, specifically excluding regions characterized by seasonal reversals in flux sign—a feature that can introduce substantial artifacts during model–data comparisons. Instead, our analysis focuses primarily on regions exhibiting robust, clear oceanic CO_2 flux signals. Recognizing that inherent uncertainties in atmospheric inversions stem from sub-grid scale anthropogenic emissions and localized sea-ice melt,; we follow the

protocols of Fay et al. (2024) and exclude both the coastal ocean and high-latitude marginal ice zones from the model-data evaluation.

Based on the spatial patterns of oceanic CO_2 outgassing, uptake, and low-flux regimes characterized in the Pacific (Fig. 2c), this study delineates 12 key regions exhibiting high air–sea CO_2 flux variability as identified by NOAA CT2022 (Fig. 2d).These are selected from the 30 ocean basins defined in the CT2022 model documentation (Jacobson et al., 2023) for optimizing flux inversions. These oceanic domains are categorized into three major basins: (1) the Pacific Ocean, (2) the Indian Ocean, and (3) the Atlantic Ocean (Table 1). Within the Pacific basin, underlined labels denote the regions exhibiting the most pronounced oceanic CO_2 outgassing (EEP) and uptake (NEP).

3. Results

3.1 The climatological mean and seasonal variations of air–sea CO_2 flux

We utilize the traditional air–sea CO_2 flux bulk formula (Eq. 1) in CESM1.2.2 while also incorporating wave and bubble-mediated effects via a gas transfer velocity parameterized by u^*, SST, and H_s (Eq. 3). A comparison of the climatological means and monthly standard deviations highlights that the spatial distribution of the model-simulated air–sea CO_2 fluxes is broadly consistent with NOAA CT2022, with regional differences generally remaining below 0.5 mol m^{-2} yr^{-1} (Figs. 2a–f). Notably, the Pacific CO_2 outgassing and uptake regions simulated by the POP2–waves experiment show smaller range-normalized relative magnitudes of model–data biases (Table 3) relative to NOAA CT2022 than the B–CTL baseline, despite a higher monthly SD in POP2–waves over both the Pacific and Indian Oceans.

To clarify our shortlisting criteria, the 12 regions were categorized based on two quantitative features:

1. Seasonal phasing consistency: Whether the simulated seasonal cycles (temporal trends) align with the NOAA CT2022 atmospheric inversion framework.

2. Relative magnitudes of model–data biases: The monthly averaged deviation as a percentage of the overall range (95% minus 5%) relative to the NOAACT2022 baseline.

The nine regions in Fig. 3 exhibit both highly coherent seasonal phasing and relatively small monthly model–data biases. In contrast, the three regions in Fig. 4 display prominent structural mismatches, such as inverted seasonal trends. Importantly, these temporal phase misalignments directly amplify the calculated monthly model–data biases, as the model and data fluctuate in opposing directions throughout the annual cycle. This phase mismatch ultimately leads to substantially larger relative monthly mean biases; specifically, the model–data biases averaged across the three regions in Fig. 4 (32.9 %) are significantly larger than those in the nine regions of Fig. 3 (27.5% in B–CTL and 23.0% in POP2–waves, respectively).

In terms of the regional mean values of air–sea CO_2 flux, the POP2–waves demonstrate closer structural agreement with NOAA CT2022 compared to the uncoupled B–CTL baseline across eight key regions (excluding the Northwest Pacific (NWP) in Fig. 3). Nevertheless, despite this larger mean offset in specific areas like the NWP, the POP2–waves successfully captured the autumn transition of oceanic CO_2 from a sink to a source as depicted in NOAA CT2022 — a feature that remains unsimulated in B–CTL. Table 3. presents the range-normalized relative magnitudes of model–data biases across nine selected regions, providing a robust metric to evaluate the simulated seawater carbonate-pH and flux field performance against the NOAA CT2022 atmospheric inversion baseline. Overall, the wave-coupled framework (POP2–waves) demonstrates a pervasive and substantial reduction in systematic biases compared to the uncoupled control simulation (B–CTL). Specifically, the regional mean absolute deviation dropped noticeably in major ocean basins, with the most

pronounced improvement captured in the Equatorial Eastern Pacific (EEP), where the relative bias was drastically attenuated by 25.0 % (from 71.5 % in B–CTL down to 46.5 % in POP2–waves. Notable bias reductions are also observed in the Northwest Pacific (NWP, down 4.9 %), South Indian Ocean Region 1 (SIO1, down 4.1%), and South Atlantic Ocean (SAO, down 4.4 %, confirming that incorporating wave-effect mechanisms successfully rectifies over- or under-estimations in air–sea carbon exchange dynamics. Conversely, the uncoupled baseline (B–CTL) slightly outperforms the coupled model only in the Equatorial Atlantic Ocean (EAO) (11.9 % vs. 15.0 %), suggesting minor localized over-compensations in wave parameterizations within this sub-basin. Nonetheless, the consistent narrowing of relative biases across the vast majority of regions firmly underscores the superior performance and statistical robustness of the online-coupled framework.

The POP2–waves simulation generally exhibits higher a SD than B–CTL, reflecting an amplified seasonal variability (Figs. 3–4). Although these SD values typically remain below 3 mol m^{-2} yr^{-1}, they peak during boreal winter, a phenomenon driven by intense oceanic CO_2 uptake in high-latitude regions of the Northern Hemisphere, such as the Northwestern and Northeastern Pacific, and North Atlantic Ocean 1. In contrast, the Southern Hemisphere exhibits pronounced monthly SD alongside robust oceanic CO_2 uptake during the austral winter (boreal summer), particularly across regions such as the South Pacific Ocean 1 (SPO1), South Indian Ocean 1 (SIO1), and South Atlantic Ocean (SAO). The monthly SD derived from NOAA CT2022 exhibits substantial regional heterogeneity. Notably, variability within the Northwest Pacific (NWP), Equatorial Eastern Pacific (EEP), and North Atlantic Ocean 1 (NAO1) exceeds that simulated by both the coupled POP2–waves model and the uncoupled control B–CTL framework.

Three specific sub-basins—the South Pacific Ocean Region 2 (SPO2), South Indian Ocean Region 2 (SIO2), and North Atlantic Ocean Region 2 (NAO2)—exhibit prominent model-data discrepancies when evaluated against NOAA CT2022 (Fig. 4). Notably, these systematic deviations are not attributable to wave-mediated processes or the parameterization of the CO_2 flux bulk formula. Within the NAO2, both B–CTL and POP2–waves models simulate a strong seasonal variations that mirrors the NAO1, characterized by robust oceanic CO_2 uptake during the boreal winter; conversely, NOAA CT2022 displays the opposite seasonal trajectory in this sub-basin. A structurally similar mismatch is observed in the mid-latitude South Pacific (SPO2), where the simulated seasonal cycles of both models exhibit strong synchronization with those in SPO1 but contrast sharply with the inverse trend captured by the NOAA CT2022 atmospheric inversion framework.

3.2 The relationship between U_{10} and $k_{w,660}$ in two regions with contrasting wind speed regimes

To demonstrate that the sea state–dependent gas transfer velocity (Deike and Melville, 2018) provides a more suitable estimate of air–sea CO_2 flux than the wind-only formulation (Wanninkhof, 1992) under high-wind conditions ($U_{10} > 10$ m s^{-1}), we selected the Western Pacific (WP) and the Equatorial Pacific (EP) regions due to their contrasting wind regimes. The WP region experiences a high frequency of high-wind conditions (exceeding 30%), whereas wind speeds in the EP region consistently remain below this threshold. Because both regions exhibit stable and significant oceanic CO_2 outgassing or uptake, they enable a clear comparative analysis of the correlation between $k_{w,660}$ and U_{10} (Figs. 5a, b).

Generally, the B–CTL data shows higher R^2 but lower $k_{w,660}$ values compared to POP2–waves $k_{w,660}$ across both the WP and EP. The POP2–waves experiment exhibits

a slightly lower R^2 than B–CTL due to greater deviations between $k_{w,660}$ and U_{10}, particularly at higher surface wind speeds. This pattern is consistent with the findings of Gutiérrez-Loza et al. (2022) under conditions where H_s > 1.5 m. The relationship between $k_{w,660}$ and U_{10} was evaluated under two scenarios: baseline monthly climatological means (H_s < 1.5m) and high-resolution daily data filtered for H_s > 1.5m (enhanced conditions) aggregated into 30-year monthly averages. Notably, both approaches substantially diminish the differences in $k_{w,660}$ at identical U_{10} values.

However, short-term (30 min) observations indicate that gas transfer velocity can be up to twice as high under similar wind speeds when H_s > 1.5 m (Gutiérrez-Loza et al., 2022. Divergence between the models becomes significant when U_{10} exceed 12 m s^{-1} over the WP region (Fig. 5a); whereas over the EP region, the convergence of $k_{w,660}$ estimates is most notable around U_{10} = 9 m s^{-1} (Fig. 5b), suggesting that mid-range wind speeds dominate the EP flux signal.

As shown in Fig. 5c, the enhanced WP cases (H_s > 1.5 m) have data available for all months except August and October, during which their $k_{w,660}$ values consistently exceed both the all-data POP2–waves and B–CTL averages. In contrast, the EP region exhibits H_s > 1.5 m data only during the summer months (July to October), where the corresponding $k_{w,660}$ values also exceed both the all-data POP2–waves and B–CTLaverage. The monthly SD indicates no significant differences between the enhanced (H_s > 1.5 m) data and the standard POP2–waves simulations over the WP, with the $k_{w,660}$ discrepancies between the two datasets remaining minimal from January to May because the average H_s during this period consistently remains below 1.5 m. However, over the EP, a pronounced discrepancy is observed between the H_s > 1.5 m condition and the all-data POP2–waves average from July to September.

3.3 Regression of CO_2 flux against U_{10} under high-wind conditions

The wind-only parameterization of gas transfer velocity tends to underestimate values under high-wind conditions ($U_{10} > 10$ m s^{-1}) or high significant wave heights ($H_s > 1.5$ m) (e.g., Gutiérrez-Loza et al., 2022; Zhou et al., 2023). Under these high-wind conditions, the monthly mean air–sea CO_2 fluxes derived from the B–CTL and POP2–waves simulations diverge notably within the Western Pacific region (WP) (Fig. 6), highlighting key discrepancies between the wind-only and wave-modified $k_{w,660}$ formulations. The data were filtered to include only grid points that met this high-wind threshold before being regionally averaged, Because not all months contained grid points satisfying the threshold, a final subset of 154 data points was utilized for the linear regression analysis. These high-wind conditions over the WP region occur primarily in winter (accounting for 42% of the valid data), when the concurrent low sea surface temperatures further enhance CO_2 solubility. The slopes of the regression equations (–0.77 mol m^{-2} yr^{-1} per m s^{-1} for B–CTL and –1.40 mol m^{-2} yr^{-1} per m s^{-1} for POP2–waves) alongside the mean CO_2 fluxes (Y_{avg}: –6.35 mol m^{-2} yr^{-1} for B–CTL and –6.97 mol m^{-2} yr^{-1} for POP2–waves) both indicate that POP2–waves a higher sensitivity to wind speed, leading to stronger oceanic CO_2 uptake across the WP domain under elevated wind speeds.

The correlation coefficient (R) of the POP2–waves simulation is higher than that of B–CTL, indicating that the sea state–dependent $k_{w,660}$ formulation provides a more robust estimate of the CO_2 flux than the wind-only $k_{w,660}$ scheme under high-wind conditions. This finding aligns with the observations of Gutiérrez-Loza et al. (2022) and Zhou et al. (2023). The average air–sea CO_2 flux in B–CTL over the WP region during DJF and JJA is −0.021 and −0.004 mol m^{-2} yr^{-1}, respectively. Meanwhile, POP2–waves exhibits only slight discrepancies relative to B–CTL during these respective seasons, with differences of more than 0.001 mol m^{-2} yr^{-1} and less than 0.002 mol m^{-2} yr^{-1} in CO_2 uptake (data not shown). This contrast

indicates that under high-wind conditions, the episodic air–sea CO_2 flux is significantly greater than the seasonal baseline averages .

3.4 Analysis of surface fields and $k_{w,660}$ component in POP2–waves and B–CTL

The spatial co-variations of sea level pressure (PSL), U_{10}, and H_s underscore their combined role as key meteorological and wave drivers steering the regional $k_{w,660}$ patterns (Figs. 7a, b). The region with $H_s > 1.5$ m is generally situated where $U_{10} > 8$ m s^{-1} and lies south of the high PSL region. The spatial patterns of climatological U_{10} and H_s align closely with the findings of Reichl and Deike (2020) (Figs. 7a, b). Furthermore, a dominance of bubble-mediated transfer in the POP2–waves simulation, where the $k_{wB,660}/k_{w,660}$ ratio exceeds 0.5, primarily occurs in regions characterized by $H_s > 1.5$ m (Fig. 7b). However, an elevated H_s does not always correspond to a higher $k_{wB,660}/k_{w,660}$ ratio in the POP2–waves simulation; this decoupling is explicitly observed in the North Pacific (Fig. 7b).

Deike and Melville (2018) demonstrated that the bubble contribution to CO_2 transfer exceeds 40% when the $U_{10} \geq 10$ m s^{-1}. In our POP2–waves simulation,the bubble fraction ($k_{wB,660}/k_{w,660}$) accounts for approximately 38% of total gas transfer velocity, which is slightly higher than ~30% reported by Reichl and Deike (2020). This discrepancy may be attributed to differences in the A_B scaling coefficients (Eq. 3), which is derived from field data, where gas transfer velocity are estimated from eddy covariance flux measurements (Reichl and Deike, 2020; Brumer et al., 2017).

The structural differences in $k_{w,660}$ (POP2–waves − B–CTL) reveal that the most pronounced discrepancies are primarily distributed in regions characterized by elevated H_s, particularly in the Southern and South Indian Oceans. (Fig. 7c). Although U_{10} in the Indian Ocean and tropical Pacific is relatively low (<5 m s^{-1}; Fig. 7a), the $k_{w,660}$ values simulated by POP2–waves remain approximately 9 cm hr^{-1} higher than

468 those in B–CTL. In these regions, this wave-driven enhancement of the total gas
469 transfer velocity is predominantly governed by the non-bubble-mediated component
470 ($k_{wNB,660}$; Fig. 7d). Although H_s is also elevated in the Southern Ocean (Fig. 7b), it
471 does not contribute substantially to the $k_{w,660}$ difference between POP2–waves and B–
472 CTL; this is because the high U_{10} in this region (Fig. 7a) already yields high gas
473 transfer velocities through the empirical formulation of Wanninkhof (1992). The
474 spatial patterns of both the B–CTL $k_{w,660}$ and the wave-induced discrepancies $k_{w,660}$
475 (POP2–waves − B–CTL) closely align with the findings of Reichl and Deike (2020)
476 (Fig. 7c). Overall, the two simulations exhibit consistent geographic distributions,
477 yielding 30-year domain-wide mean gas transfer velocities of 17.0 cm hr^{-1} for B–CTL
478 and 22.7 cm hr^{-1} for POP2–waves, despite their reliance on distinct input parameters
479 (U_{10} vs. u^* and H_s). Aside from the polar regions, the total gas transfer velocity in the
480 POP2–waves coupled model exceeds that in B–CTL, with the most pronounced
481 differences localized in the tropics (Fig. 7c). To elucidate the driving mechanisms
482 behind this global enhancement, it is necessary to quantify whether the non-bubble
483 ($k_{wNB,660}$) or bubble-mediated ($k_{wB,660}$) component dominates the total gas transfer
484 velocity across the different ocean basins. These discrepancies reveal a dominance of
485 bubble-mediated transfer ($k_{wB,660} > k_{wNB,660}$) under elevated H_s regimes, contrasting
486 with a shift toward non-bubble dominance ($k_{wB,660} < k_{wNB,660}$) in regions where 10-m
487 wind speeds remain below 7 m s^{-1} (Fig. 7).
488
489 **3.5 Mean State and model differences in pCO_2^w and surface pH**
490 Integrating wave dynamics induces a pronounced spatial reorganization of both
491 pCO_2^w and ocean surface pH over the 30-year climatological period (Fig. 8).
492 Specifically, the baseline B–CTL simulation shows that high pCO_2^w is concentrated in
493 the equatorial eastern Pacific (EEP), contributing to a larger oceanic CO_2 source (Fig.

494 8a). In contrast, low pCO_2^w is found in high-latitude regions of the Pacific and Atlantic
495 (e.g., NWP, NEP, NAO1, and NAO2), driving strong oceanic CO_2 uptake (Fig. 8a).
496 Over the study period, the climatological standard deviation of pCO_2^w in the B–CTL
497 simulation fluctuates between 10 and 30 ppm (Fig. 8a).

498 In the CESM1 framework of the B_2000_CAM5 compsets, atmospheric pCO_2^a is
499 held constant (367 ppm). The pCO_2^w in the Eastern Pacific exceeds 440 ppm, indicating
500 an air–sea $dpCO_2$ greater than 73 ppm in B–CTL (109.8 and 92.7 ppm during DJF and
501 JJA, respectively), whereas the pCO_2^w in the Western Pacific is below 320 ppm,
502 indicating an air–sea $dpCO_2$ lower than −47 ppm (−53.4 and −31.4 ppm during DJF
503 and JJA, respectively). Notably, POP2–waves reduces the high pCO_2^w by more than
504 10 ppm over the Eastern Equatorial Pacific and increases the low pCO_2^w in other
505 regions (Fig. 8b). Consequently, in the oceanic CO_2 outgassing (uptake) regions, the
506 POP2–waves coupled model decreases (increases) pCO_2^w, thereby reducing the
507 magnitude of the air–sea $dpCO_2$. The SD of the pCO_2^w difference between POP2–waves
508 and B–CTL varies significantly in Eastern Equatorial Pacific, while SD changes in
509 other regions are less pronounced.

510 The biogeochemical module of POP2 (MARBL) updates TA in each grid cell by
511 solving a coupled transport–reaction equation (Long et al., 2021). The average pH of
512 the ocean is currently around 8.1 in oceanic CO_2 uptake regions (e.g., the Western
513 Pacific) and 8.0 in outgassing regions (e.g., the Equatorial Pacific, Fig. 8c), reflecting
514 slightly alkaline conditions. Within the DIC system, bicarbonate ions (HCO_3^-) are the
515 dominant species because the prevailing seawater pH lies between pK_{a1} and pK_{a2}.
516 However, continued uptake of atmospheric CO_2 drives a decline in pH—a process
517 termed ocean acidification. Our study highlights that wave-induced $k_{w,660}$ significantly
518 influences the marine CO_2 system, altering alkalinity, pH, and carbonate speciation.
519 These chemical shifts, in turn, provide a feedback mechanism that modulates the overall

dynamics of the air–sea CO_2 flux. In other words, perturbations in $k_{w,660}$ influence both $dpCO_2$ and air–sea CO_2 flux within the Earth System Model.

Ocean pH and surface ocean pCO_2^w are strongly negatively correlated (Macovei et al. 2021). Consequently, low pH values are observed in the Equatorial Eastern Pacific (Fig. 8c), as a direct result of the elevated DIC and pCO_2^w concentrations characteristic of that region (Fig. 8a). Conversely, higher pH values are sustained in regions exhibiting lower pCO_2^w levels, a feature predominantly found across the high-latitude domains of both the Pacific and Atlantic Oceans. Rustogi et al. (2025) indicate that accelerated equilibration of oceanic pCO_2 in the wind–wave–bubble simulation, driven by enhanced gas exchange, ultimately reduces the magnitude of the air–sea $dpCO_2$. This pCO_2 feedback is strongest in the extratropics, where it suppresses CO_2 uptake. Our POP2–waves experiment reveals a consistent response, characterized by increasing in both oceanic pCO_2 (Fig. 8b) and hydrogen ion concentration, which are accompanied by a corresponding decline in pH (Fig. 8d) across the extratropics. Accounting for wave effects results in simulated pH shifts of approximately + (-) 0.01 in oceanic CO_2 outgassing (uptake) regions (Fig. 8d). This suggests that incorporating this mechanism alleviates acidification in the equatorial Pacific, whereas it intensifies ocean acidification in the high-latitude domains of both the Pacific and Atlantic Oceans (Fig. 8d). Rustogi et al. (2025) also showed that the effects of Δk_w (the difference between wave-induced and based on U_{10}) and $\Delta dpCO_2$ partially offset each other. However, because the Δk_w effect is generally 20%–30% stronger, it dominates the counteracting $\Delta dpCO_2$ effect, explaining the modest increase observed in both oceanic outgassing and uptake CO_2 regions within the wave-effect simulation.

4. Discussion

4.1 Impact of wave-dependent k_w on global air–sea CO_2 flux: a comparison between POP2–waves and standard Earth System Models

Several investigations have parameterized the air–sea CO_2 flux using Eq. (1), yet current $k_{w,660}$ parameterizations within prominent global frameworks still rely exclusively on the neutral 10-m wind speed (U_{10}) as seen in models such as MPI-ESM1.2 (Mauritsen et al., 2019), CESM2 (Danabasoglu et al., 2020), NorESM2 (Seland et al., 2020), UKESM1 (Ziehn et al., 2020), MIROC6 (Chikamoto and DiNezio, 2021), CMCC-ESM2 (Lovato et al., 2022), and CanESM5 (Sigmond et al., 2023) (Table 2). Concurrently, pioneering efforts have begun quantifying wave-induced effects on both air–sea CO_2 flux and long-term ocean carbon storage by incorporating coupled wind–wave–bubble gas transfer formulations into the Ocean general circulation models (OGCMs), such as MOM6–COBALTv2 (Rustogi et al., 2025) and NEMO–PISCES (Wu et al., 2025). Notably, Wu et al. (2025) underscore that integrating these wave-mediated boundary layer dynamics into comprehensive Earth System Models is essential for reducing systemic uncertainties in global carbon cycle projections.

Several studies have incorporated wave effects following the parameterization of Deike and Melville (2018), utilizing the Surface Ocean CO_2 Atlas (SOCAT) database (Bakker et al., 2016) to calculate diagnostic air–sea CO_2 fluxes. In these offline configurations, however, the computed air–sea CO_2 flux is treated independently of pCO_2^w dynamics and surface pH evolution, lacking any interactive feedback mechanisms between the atmosphere and the upper-ocean carbonate system.

Rustogi et al. (2025) utilized an ocean-biogeochemistry system forced by offline atmospheric reanalysis and wave model outputs. While comprehensive, such an offline-forced setup is limited in its ability to capture high-frequency, episodic, and synchronous interactions between physical wave states and surface water chemistry

571 during rapid weather transitions. In contrast, our study implements an online coupling
572 framework. The key value-add of our setup is its capacity to simulate step-by-step,
573 interactive feedbacks where wave properties dynamically alter the gas transfer
574 velocity ($k_{w,660}$) and physical mixing in real-time. The coupled behavior of POP2–
575 waves includes $dpCO_2$-driven negative feedbacks, which fundamentally differs from
576 traditional obs-based products, that treat wave-induced $k_{w,660}$ and $dpCO_2$ as
577 independent variables when estimating air–sea CO_2 flux (e.g., Reichl and Deike,
578 2020). This online coupling mechanism also contrasts with global ocean model forced
579 offline by atmospheric reanalysis and wave model outputs (e.g., Rustogi et al., 2025),
580 where such interactive feedbacks are often omitted. This allows our model to capture
581 non-linear, high-resolution impacts on the air–sea CO_2 flux during highly dynamic
582 conditions, which are often smoothed out in offline-forced simulations.
583
584 **4.2 Impact of air–sea $dpCO_2$, $k_{w,660}$, SST, and pH on air–sea CO_2 flux**
585 To evaluate which driver exerts the most direct control on air–sea CO_2 flux, Fig.
586 9 displays the spatial distributions of the linear regression coefficients (LRCs)
587 between the flux and various standardized variables: air–sea $dpCO_2$ (Fig. 9a), $k_{w,660}$
588 (Fig. 9b), SST (Fig. 9c), and pH (Fig. 9d). To remove the confounding artifacts of
589 differing physical units and enable a direct comparison on a common scale, both the
590 air–sea CO_2 flux and the independent variables were standardized into anomalies
591 (with a mean of 0 and a standard deviation of 1) prior to the regression analysis. The
592 statistical significance of these regressed relationships was subsequently evaluated
593 using a Student's t-test at the 95% confidence level. This standardization constraints
594 the LRCs to range strictly between −1 and +1. Here, we do not delve into the intricate
595 chemical and biochemical feedback mechanisms governing carbonate species.
596 Nevertheless,, it is worth noting that the collective influence of carbonate

composition—specifically TA, and dissolved inorganic carbon (DIC)—on pCO_2^w variability has been shown to outweigh that of solubility changes driven by sea surface salinity and SST (e.g., Koseki et al., 2023).

Among these drivers,, air–sea $dpCO_2$ and air–sea CO_2 flux exhibit the strongest positive LRCs, with coefficients ranging from 0.6 to 0.8 across the global ocean; this underscores the role of the ocean acting as net CO_2 source or sink depending on the sign of the air–sea $dpCO_2$ gradient. Additionally, wave effects increase the LRCs by approximately 0.1 to 0.2, particularly within regions of intense oceanic CO_2 outgassing or uptake. A clear positive (negative) LRCs exists between $k_{w,660}$ and the air–sea CO_2 flux in oceanic CO_2 outgassing (uptake) regions. Furthermore, wave effects reduce the absolute LRCs between $k_{w,660}$ and air–sea CO_2 flux in both oceanic CO_2 outgassing (uptake) regions (Fig. 9b). This indicates that once interactions between the modeled CO_2 flux and the ocean carbonate-pH system are considered, the wave-influenced CO_2 flux becomes less correlated with $k_{w,660}$ and more closely linked to air–sea $dpCO_2$. This shift can be attributed to the limitations of wind-only parameterizations; as indicated by Zhou et al. (2023), wind-only formulas tend to underestimate gas transfer velocities when U_{10} exceeds 10 m s^{-1}, whereas enhanced gas transfer velocity frequently occurs under conditions of strong wave breaking and high significant wave height. Johansson et al. (2022) reported that H_s generally increases with wind speed, but the relationship is strongly modulated by wind direction and regional conditions, leading to spatially variable and nonlinear wind–wave coupling.

In contrast to the former, there is a clear positive (negative) LRCs between SST and CO_2 flux in oceanic CO_2 uptake (outgassing) regions (Fig. 9c). A negative correlation exists between $k_{w,660}$ and SST, reflecting the latitudinal gradient where colder, high-latitude waters are characterized by more intense sea states and elevated

623 $k_{w,660}$ values. This pattern occurs because lower temperatures at high latitudes increase
624 CO_2 solubility (Séférian et al., 2020), thereby enhancing oceanic uptake. As SST
625 increases, the kinetic energy of CO_2 molecules in seawater rises, enhancing their
626 diffusion and consequently reducing the Schmidt number (Sc = ν/D, defined as the
627 ratio of kinematic viscosity to the molecular diffusion coefficient). Because $k_{w,660}$ is
628 parameterized as a function of $Sc^{-0.5}$, a decrease in Sc leads to an increase in both
629 $k_{w,660}$ and net air–sea CO_2 flux. Fay et al. (2024) attributed the discrepancies and
630 variations in air–sea CO_2 fluxes to a combination of factors, including choices in wind
631 speed products, SST datasets, biological carbon uptake, and the parameterization of
632 gas transfer velocity. Wave effects only slightly reduce the LRCs between SST and
633 the air–sea CO_2 flux—by approximately 0.1—within the tropics, with negligible
634 impacts observed in other regions. The strong negative correlation between ocean pH
635 and pCO_2^w is dictated by the acid dissociation equilibria of the marine carbonate
636 system (Fig. 8a, c), which govern the fundamental relationship between dissolved
637 CO_2 and hydrogen ion concentration (Williams et al., 2017). As seawater pH
638 decreases, the resulting increase in hydrogen ion ($[H^+]$) concentration drives a reaction
639 with carbonate ions (CO_3^{2-}). This consumption of carbonate ions ultimately reduces
640 the ocean's buffering capacity for CO_2 uptake. Consequently, pCO_2^w increases and
641 $dpCO_2$ decreases, suppressing the air–sea CO_2 flux into the ocean. Reflecting this
642 mechanism, pH and air–sea CO_2 flux exhibit strong negative LRCs (less than –0.9)
643 across most of the global ocean, with exceptions limited to the Eastern Equatorial
644 Pacific and along the Arctic margins (Fig. 9d). Wave effects marginally attenuate this
645 relationship in the Eastern Equatorial Pacific (EEP), reducing the LRCs by
646 approximately 0.1.
647

4.3 Uncertainty arising from the absence of interactions between air–sea CO_2 flux and the ocean carbonate–pH system

Rustogi et al. (2025) indicate that as surface seawater pCO_2^w responds to changes in DIC and alkalinity, the air–sea $dpCO_2$ gradient is partially attenuated. This induces a negative feedback loop whereby enhanced CO_2 uptake (or outgassing) is systematically damped by chemical re-equilibration within the marine carbonate system, a mechanism that is highly consistent with the findings of this study. To assess the uncertainty in CO_2 flux resulting from the absence of interactions between the flux and the ocean carbonate–pH system (i.e., the decoupling of the $dpCO_2$-driven negative feedback). The air–sea CO_2 flux was reconstructed using the uncoupled $dpCO_2$ fields from the control simulation (B–CTL) and alongside the wave-influenced $k_{w,660}$ parameterization from the coupled wave simulation (POP2–waves). This experimental setup explicitly isolates the statistical mean and standard deviation of the flux under a scenario defined by the "lack of $dpCO_2$-driven negative feedback". Only data significant at a 95% confidence level of air–sea CO_2 flux difference between "lack of $dpCO_2$-driven negative feedback" and POP2–waves are shown in Fig. 10b. Compared to the baseline (Fig. 2b), the CO_2 flux in the "lack of $dpCO_2$-driven negative feedback" scenario is stronger than that in the POP2–waves simulation across both oceanic CO_2 outgassing and uptake regions, accompanied by a larger SD. The most pronounced discrepancies occur in the Pacific basin across both outgassing and uptake zones. However, certain mid-to-high latitude subregions—specifically the Northeastern Pacific (NEP), South Indian Ocean 2 (SIO2), and South Pacific Ocean 2 (SPO2)—do not reach the 95% confidence threshold.

Rustogi et al. (2025) demonstrate that while wave-enhanced $k_{w,660}$ accelerates local air–sea CO_2 exchange, it simultaneously attenuates the air–sea $dpCO_2$ gradient. In this study, we conceptualize this process as a manifestation of the ocean's buffering

capacity, which encompasses the dynamic coupling between CO_2 flux (estimated via $k_{w,660}$) and the marine carbonate–pH system. Within the coupled POP2–waves framework, incorporating wave effects alleviates surface acidification and reduces air–sea $dpCO_2$ over oceanic CO_2 outgassing regions; conversely, the resulting relatively higher pH levels systematically enhance the ocean's capacity to absorb atmospheric CO_2 within regions characterized by oceanic CO_2 uptake region in the coupled POP2–waves model. In contrast, the simulation lacking the $dpCO_2$-driven negative feedback—artificially omits realistic marine buffering effects—overestimates the air–sea exchange, yielding excess CO_2 outgassing into the atmosphere (>0.4 mol m^{-2} yr^{-1}) over source regions. Concurrently, it amplifies excess CO_2 uptake (<−0.4 mol m^{-2} yr^{-1}) within regions characterized by oceanic CO_2 uptake regions (Fig. 10b) compared to the coupled POP2–waves model.

5 Conclusions

The study advances Earth System Model by developing an online coupling framework (POP2–waves) that incorporates wave effects directly into air–sea CO_2 flux simulations, effectively capturing the $dpCO_2$-driven negative feedback in the marine carbonate-pH system. Neglecting this coupling by treating $dpCO_2$ and wave-induced $k_{w,660}$ independently leads to a substantial overestimation of global fluxes. Fully integrating these wave effects into ocean biogeochemical models addresses three grand challenges in climate modeling:

1. Technical implementation: Resolving coordinate interpolation, boundary discontinuities in wave energy, and MPI parallelization.
2. Interdisciplinary analysis: Harmonizing kinematic, thermodynamic, and biogeochemical frameworks across distinct Earth system components.

3. Validation constraints: Overcoming sparse observational data by synthesizing indirect flux estimates from atmospheric inversions (e.g., NOAA CT2022), ships, and buoys.

Within the coupled POP2–waves framework, the gas transfer velocity is resolved using the parameterization of Deike and Melville (2018), which attributes bubble-mediated transfer to the combined effects of friction velocity and significant wave height. This setup extends the framework of Wu et al. (2025) by utilizing a dynamically coupled ocean–wave system. This advanced coupling explicitly captures how flux-driven alterations in surface $dpCO_2$ feedback nonlinearly via the interactive interface to modulate the global air–sea CO_2 flux itself. Our regional evaluation reveals a mixed and basin-dependent performance when introducing wave effects. Across the majority of the 12 key regions of high variability defined by NOAA CT2022, the POP2–waves simulation shows a closer structural agreement with the inversion data compared to the uncoupled B–CTL baseline. However, this improvement is not universal; notable discrepancies persist within specific sectors, including the South Pacific Ocean 2, South Indian Ocean 2, and North Atlantic Ocean 2, where the wave-coupled model does not clearly outperform the baseline.

Significant deviations between POP2–waves and B–CTL simulations emerge when significant wave height exceeds 1.5 m. Consistent with Gutiérrez-Loza et al. (2022), this wave-induced divergence results in a systematically air–sea CO_2 flux under high 10-m wind speed and significant wave height. Across the entire spatiotemporal domain, the bubble-mediated contribution to the total gas transfer velocity ($k_{wB,660}/k_{w,660}$) in POP2–waves averages approximately 38%. This finding slightly exceed the ~30% baseline reported by Reichl and Deike (2020). These high $k_{wB,660}/k_{w,660}$ ratios align with regions of elevate 10-m wind speed and significant wave height. Concurrently, our results indicate that bubbles-mediated processes account for up to 41.3% of the total

725 air–sea CO_2 flux, which is consistent with the ~40% contribution reported by both
726 Reichl and Deike (2020) and Zhou et al. (2023).

727 Within oceanic CO_2 outgassing regions, POP2–waves attenuates the high air–sea
728 $dpCO_2$ gradient, whereas it enhances low gradients elsewhere. This feedback drives
729 surface pH shifts of approximately±0.01 that spatially align with the sign of regional
730 flux. On a global scale, the air–sea $dpCO_2$ (pH) displays the strongest positive (negative)
731 regression coefficients with the flux. Additionally, while gas transfer velocity scales
732 positively with the absolute air–sea CO_2 flux magnitude, whereas SST demonstrates an
733 inverse relationship to this gas transfer velocity sensitivity.

734 Compared to the B–CTL baseline, POP2–waves simulations show that oceanic
735 CO_2 uptake and outgassing regions expand by 11.8% and 41.6%, respectively, resulting
736 in a 1.8% increase in the global ocean CO_2 sink. Consequently, while wave-induced
737 enhancements in $k_{w,660}$ boost instantaneous air–sea CO_2 flux, the coupled carbonate–pH
738 system limits the net long-term impact via this this $dpCO_2$-driven feedback (Rustogi et
739 al., 2025). This feedback decouples local increases in CO_2 flux from proportional
740 proportional changes in the global mean ocean carbon sink.

741 The impacts of the $k_{w,660}$ bulk formula (Wanninkhof et al., 1992) and wave
742 dynamics (Deike and Melville, 2018) on air–sea CO_2 flux, surface pH, and air–sea
743 $dpCO_2$ are schematically summarized in Fig. 11. The B–CTL baseline captures a
744 pronounced seasonal contrast in Western Pacific air–sea CO_2 fluxes, characterized by
745 strong uptake during DJF that is heavily suppressed in JJA due to SST-driven reductions
746 in solubility. This seasonal variability in air–sea $dpCO_2$, activates a negative feedback
747 loop with the POP2–waves framework , which ultimately modulate the overall air–sea
748 CO_2 flux. Conversely, the Equatorial Pacific region exhibits lower pH than the Western
749 Pacific and acts as a persistent CO_2 source across both seasons, showing no significant,
750 with no obvious seasonal variation, a finding consistent with Fay et al. (2024).

While the current POP2–waves framework demonstrates the critical importance of online coupling and dpCO_2-driven feedbacks, several avenues remain for future model refinement. A key priority is the continuous improvement of gas transfer velocity formulations. Future efforts will focus on transitioning to the new generalized formulation proposed by Deike et al. (2025), which incorporates updated coefficients and accounts for an asymmetric bubble flux contribution. While this advancement is expected to have a minor impact on oceanic CO_2 flux estimations, it holds potential significance for constraining global marine O_2 fluxes. Furthermore, moving toward a fully coupled Earth System Model (ESM)—which integrates dynamic atmospheric feedback alongside ocean and wave components—will be essential to fully unravelling the long-term impacts of wave-induced processes on global marine biogeochemical cycles.

Code and data availability. The model code of POP2–waves coupled model is available at https://doi.org/10.5281/zenodo.15795234 (Lan, 2025). Input data of POP2–waves using the climatological Hadley Centre Sea Ice and Sea Surface Temperature dataset, including 30-year numerical experiments, are available at https://doi.org/10.5281/zenodo.5510795 (Lan et al., 2021). CarbonTracker CT2022 data are provided by the National Oceanic and Atmospheric Administration (NOAA) and available from Global Monitoring Laboratory https://gml.noaa.gov/aftp/products/carbontracker/co2/CT2022/ (Jacobson et al., 2023).

Author contributions. YYL is the sole developer of the POP2–waves coupled model and writes the majority part of the paper. HHH provides computational support and analysis suggestions. WLL supports reorganization and offers analytical recommendations and SC offers a non-parallel wave module as part of the POM source

code.

Competing interests. The authors declare that they have no conflict of interest.

Acknowledgements. Our deepest gratitude goes to the editors and anonymous reviewers for their careful work and thoughtful suggestions that have helped improve this paper substantially. We would like to thank NOAA GML (Boulder, Colorado, USA) for providing the CarbonTracker CT2022 data from the website at http://carbontracker.noaa.gov (last access: 20 May 2026). We sincerely thank the National Center for Atmospheric Research (NCAR) and their Atmosphere Model Working Group (AMWG) for releasing CESM1.2.2. We are also grateful to the National Center for High- performance Computing, Taiwan for providing the facilities for the computational procedures for running POP2–waves simulations. Thanks, Gemini and ChatGPT for correcting the English grammar.

Financial support. This research received funding from the Taiwan National Science and Technology Council under Grants NSTC 112-2111-M-001-008 and MOST 111-2123-M-001-007, as well as support from the Academia Sinica Grand Challenge Program in Taiwan under Grant AS-GCP-112-M03.

Reference

Akhand, A., Chanda, A., Watanabe, K., Das, S., Tokoro, T., Hazra, S., and Kuwae, T.: Reduction in riverine freshwater supply changes inorganic and organic carbon dynamics and air-water CO_2 fluxes in a tropical mangrove dominated estuary, J. Geophys. Res. G: Biogeosciences, 126, e2020JG006144, https://doi.org/10.1029/2020JG006144, 2021.

Andreas, E., Vlahos, P., and Monahan, E.: The potential role of sea spray droplets in facilitating air–sea gas transfer, in: IOP conference series: earth and environmental science, Vol. 35, p. 012003, IOP

Publishing, https://doi.org/10.1088/1755-1315/35/1/012003, 2016.

Bakker, D. C. E., Pfeil, B., Landa, C. S., Metzl, N., O'Brien, K. M., Olsen, A., Smith, K., Cosca, C., Harasawa, S., Jones, S. D., Nakaoka, S., Nojiri, Y., Schuster, U., Steinhoff, T., Sweeney, C., Takahashi, T., Tilbrook, B., Wada, C., Wanninkhof, R., Alin, S. R., Balestrini, C. F., Barbero, L., Bates, N. R., Bianchi, A. A., Bonou, F., Boutin, J., Bozec, Y., Burger, E. F., Cai, W.-J., Castle, R. D., Chen, L., Chierici, M., Currie, K., Evans, W., Featherstone, C., Feely, R. A., Fransson, A., Goyet, C., Greenwood, N., Gregor, L., Hankin, S., Hardman-Mountford, N. J., Harlay, J., Hauck, J., Hoppema, M., Humphreys, M. P., Hunt, C. W., Huss, B., Ibánhez, J. S. P., Johannessen, T., Keeling, R., Kitidis, V., Körtzinger, A., Kozyr, A., Krasakopoulou, E., Kuwata, A., Landschützer, P., Lauvset, S. K., Lefèvre, N., Lo Monaco, C., Manke, A., Mathis, J. T., Merlivat, L., Millero, F. J., Monteiro, P. M. S., Munro, D. R., Murata, A., Newberger, T., Omar, A. M., Ono, T., Paterson, K., Pearce, D., Pierrot, D., Robbins, L. L., Saito, S., Salisbury, J., Schlitzer, R., Schneider, B., Schweitzer, R., Sieger, R., Skjelvan, I., Sullivan, K. F., Sutherland, S. C., Sutton, A. J., Tadokoro, K., Telszewski, M., Tuma, M., van Heuven, S. M. A. C., Vandemark, D., Ward, B., Watson, A. J., and Xu, S.: A multi-decade record of high-quality fCO_2 data in version 3 of the Surface Ocean CO_2 Atlas (SOCAT), Earth Syst. Sci. Data, 8, 383–413, https://doi.org/10.5194/essd-8-383-2016, 2016.

Bange, H. W., Mongwe, P., Shutler, J. D., Arévalo-Martínez, D. L., Bianchi, D., Lauvset, S. K., Liu, C., Löscher, C. R., Martins, H., Rosentreter, J. A., Schmale, O., Steinhoff, T., Upstill-Goddard, R. C., Wanninkhof, R., Wilson, S. T., and Xie, H.: Advances in understanding of air–sea exchange and cycling of greenhouse gases in the upper ocean, Elem Sci Anth, 12 (1), https://doi.org/10.1525/elementa.2023.00044, 2024.

Behncke, J., Landschützer, P., and Tanhua, T.: A detectable change in the air–sea CO_2 flux estimate from sailboat measurements, Sci. Rep., 14, 3345, https://doi.org/10.1038/s41598-024-53159-0, 2024.

Bell, T. G., Landwehr, S., Miller, S. D., de Bruyn, W. J., Callaghan, A. H., Scanlon, B., Ward, B., Yang, M., and Saltzman, E. S.: Estimation of bubble-mediated air–sea gas exchange from concurrent DMS and CO_2 transfer velocities at intermediate–high wind speeds, Atmos. Chem. Phys., 17, 9019–9033, https://doi.org/10.5194/acp-17-9019-2017, 2017.

Blomquist, B. W,, Brumer, S. E., Fairall, C. W., Huebert, B. J., Zappa, C. J., Brooks, I. M., Yang, M., Bariteau, L., Prytherch, J., Hare, J. E., Czerski, H., Matei, A., and Pascal, R. W.: Wind speed and sea state dependencies of air–sea gas transfer: Results from the High Wind speed Gas exchange Study (HiWinGS), J. Geophys. Res.-Ocean., 122, 8034–8062, https://doi.org/10.1002/2017JC013181, 2017.

Blumberg, A. F., and Mellor, G. L.: A Description of a Three-Dimensional Coastal Ocean Circulation Model, Costal and Estuarine Science, vol. 4, American Geophysical Union, https://doi.org/10.1029/CO004p0001, 1987.

Boucher, O., Servonnat, J., Albright, A. L., Aumont, O., Balkanski, Y., Bastrikov, V., Bekki, S., Bonnet, R., Bony, S., Bopp, L., Braconnot, P., Brockmann, P., Cadule, P., Caubel, A., Cheruy, F., Codron, F., Cozic, A., Cugnet, D., D'Andrea, F., Davini, P., de Lavergne, C., Denvil, S., Deshayes, J., Devilliers, M., Ducharne, A., Dufresne, J.-L., Dupont, E., Éthé, C., Fairhead, L., Falletti, L., Flavoni, S., Foujols, M.-A., Gardoll, S., Gastineau, G., Ghattas, J., Grandpeix, J.-Y., Guenet, B., Guez, Lionel, E., Guilyardi, E., Guimberteau, M., Hauglustaine, D., Hourdin, F., Idelkadi, A., Joussaume, S., Kageyama, M., Khodri, M., Krinner, G., Lebas, N., Levavasseur, G., Lévy, C., Li, L., Lott, F., Lurton, T., Luyssaert, S., Madec, G., Madeleine, J.-B., Maignan, F., Marchand, M., Marti, O., Mellul, L., Meurdesoif, Y., Mignot, J., Musat, I., Ottlé, C., Peylin, P., Planton, Y., Polcher, J., Rio, C., Rochetin, N., Rousset, C., Sepulchre, P., Sima, A., Swingedouw, D., Thiéblemont, R., Traore, A. K., Vancoppenolle, M., Vial, J., Vialard, J., Viovy, N., and Vuichard, N.: Presentation and Evaluation of the IPSL-CM6A-LR Climate Model, J. Adv. Model. Earth Sy., 12, e2019MS002010, https://doi.org/10.1029/2019MS002010, 2020.

Brumer, S. E., Zappa, C. J., Blomquist, B. W., Fairall, C. W., Cifuentes-Lorenzen, A., Edson, J. B., Brooks, I. M., and Huebert, B. J.: Wave-related Reynolds number parameterizations of CO_2 and DMS transfer velocities, Geophys. Res. Lett., 44, 9865–9875, https://doi.org/10.1002/2017GL074979, 2017.

Chikamoto, M. O., and DiNezio, P.: Multi-century changes in the ocean carbon cycle controlled by the tropical oceans and the Southern Ocean, Global Biogeochem. Cy., 35, e2021GB007090, https://doi.org/10.1029/2021GB007090, 2021.

Chikamoto, M. O., DiNezio, P., and Lovenduski, N.: Long-term slowdown of ocean carbon uptake by alkalinity dynamics, Geophys. Res. Lett., 50, e2022GL101954, https://doi.org/10.1029/2022GL101954, 2023.

Coggins, A., Watson, A. J., Schuster, U., Mackay, N., King, B., McDonagh, E., and Poulton, A. J.: Surface ocean carbon budget in the 2017 South Georgia diatom bloom: Observations and validation of profiling biogeochemical argo floats, Deep-Sea Res. II: Top. Stud. Oceanogr., 209, 105275. https://doi.org/10.1016/j.dsr2.2023.105275, 2023.

Couldrey, M. P., Oliver, K. I. C., Yool, A., Halloran, P. R., and Achterberg, E. P.: On which timescales do gastransfer velocities control NorthAtlantic CO_2 flux variability?, Global Biogeochem. Cy., 30,787–802, https://doi.org/10.1002/2015GB005267, 2016.

Czerski, H., Brooks, I. M., Gunn, S., Pascal, R., Matei, A., and Blomquist, B.: Ocean bubbles under high wind conditions – Part 2: Bubble size distributions and implications for models of bubble dynamics, Ocean Sci., 18, 587–608, https://doi.org/10.5194/os-18-587-2022, 2022.

Danabasoglu, G., Lamarque, J.-F., Bacmeister, J., Bailey, D. A., DuVivier, A. K., Edwards, J., Emmons, L. K., Fasullo, J., Garcia, R., Gettelman, A., Hannay, C., Holland, M. M., Large, W. G., Lauritzen, P. H., Lawrence, D. M., Lenaerts, J. T. M., Lindsay, K., Lipscomb, W. H., Mills, M. J., Neale, R., Oleson, K. W., Otto-Bliesner, B., Phillips, A. S., Sacks, W., Tilmes, S., van Kampenhout, L., Vertenstein, M., Bertini, A., Dennis, J., Deser, C., Fischer, C., Fox-Kemper, B., Kay, J. E., Kinnison, D., Kushner, P. J., Larson, V. E., Long, M. C., Mickelson, S., Moore, J. K., Nienhouse, E., Polvani, L., Rasch, P. J., and Strand, W. G.: The Community Earth System Model Version 2 (CESM2), J. Adv. Model. Earth Sy., 12, e2019MS001916, https://doi.org/10.1029/2019MS001916, 2020.

Deike, L., and Melville, W. K.: Gas transfer by breaking waves, Geophys. Res. Lett., 45, 10,482–10,492. https://doi.org/10.1029/2018GL078758, 2018.

Deike, L.: Mass transfer at the ocean-atmosphere interface: The role of wave breaking, droplets, and bubbles, Annu. Rev. Fluid Mech, 54, 191–224, https://doi.org/10.1146/annurev-fluid-030121-014132, 2022.

Deike, L., Zhou, X., Rustogi, P., Stanley, R. H. R., Reichl, B. G., Bushinsky, S. M., and Resplandy, L.: A universal wind–wave–bubble formulation for air–sea gas exchange and its impact on oxygen fluxes, Proc. Natl. Acad. Sci. U.S.A., 122, e2419319122, https://doi.org/10.1073/pnas.2419319122, 2025.

Dickson, A. G.: An exact definition of total alkalinity and a procedure for the estimation of alkalinity and total inorganic carbon from titration data, Deep-Sea Res., 28A (6), 609-623, https://doi.org/10.1016/0198-0149(81)90121-7, 1981.

Dong, Y., Yang, M., Bakker, D. C. E., Kitidis, V., and Bell, T. G.: Uncertainties in eddy covariance air–sea CO_2 flux measurements and implications for gas transfer velocity parameterisations, Atmos. Chem. Phys., 21, 8089–8110, https://doi.org/10.5194/acp-21-8089-2021, 2021.

Dong, Y., Bakker, D. C. E., Bell, T. G., Huang, B., Landschützer, P., Liss, P. S., and Yang, M.: Update on the temperature corrections of global air–sea CO_2 flux estimates, Global Biogeochem. Cy., 36, e2022GB007360, https://doi.org/10.1029/2022GB007360, 2022.

Edson, J. B., Fairall, C. W., Bariteau, L., Zappa, C. J., Cifuentes-Lorenzen, A., McGillis, W. R., Pezoa, S., Hare, J. E., and Helmig, D.: Direct covariance measurement of CO_2 gas transfer velocity

during the 2008 Southern Ocean Gas Exchange Experiment: Wind speed dependency, J. Geophys. Res., 116, https://doi.org/10.1029/2011jc007022, 2011.

Fay, A. R., Gregor, L., Landschützer, P., McKinley, G. A., Gruber, N., Gehlen, M., Iida, Y., Laruelle, G. G., Rödenbeck, C., Roobaert, A., and Zeng, J.: SeaFlux: harmonization of air–sea CO_2 fluxes from surface pCO_2 data products using a standardized approach, Earth Syst. Sci. Data, 13, 4693–4710, https://doi.org/10.5194/essd-13-4693-2021, 2021.

Fay, A. R., Munro, D. R., McKinley, G. A., Pierrot, D., Sutherland, S. C., Sweeney, C., and Wanninkhof, R.: Updated climatological mean ΔfCO_2 and net sea–air CO_2 flux over the global open ocean regions, Earth Syst. Sci. Data, 16, 2123–2139, https://doi.org/10.5194/essd-16-2123-2024, 2024.

Friedlingstein, P., Jones, M. W., O'Sullivan, M., Andrew, R. M., Bakker, D. C. E., Hauck, J., Le Quéré, C., Peters, G. P., Peters, W., Pongratz, J., Sitch, S., Canadell, J. G., Ciais, P., Jackson, R. B., Alin, S. R., Anthoni, P., Bates, N. R., Becker, M., Bellouin, N., Bopp, L., Chau, T. T. T., Chevallier, F., Chini, L. P., Cronin, M., Currie, K. I., Decharme, B., Djeutchouang, L. M., Dou, X., Evans, W., Feely, R. A., Feng, L., Gasser, T., Gilfillan, D., Gkritzalis, T., Grassi, G., Gregor, L., Gruber, N., Gürses, Ö., Harris, I., Houghton, R. A., Hurtt, G. C., Iida, Y., Ilyina, T., Luijkx, I. T., Jain, A., Jones, S. D., Kato, E., Kennedy, D., Klein Goldewijk, K., Knauer, J., Korsbakken, J. I., Körtzinger, A., Landschützer, P., Lauvset, S. K., Lefèvre, N., Lienert, S., Liu, J., Marland, G., McGuire, P. C., Melton, J. R., Munro, D. R., Nabel, J. E. M. S., Nakaoka, S.-I., Niwa, Y., Ono, T., Pierrot, D., Poulter, B., Rehder, G., Resplandy, L., Robertson, E., Rödenbeck, C., Rosan, T. M., Schwinger, J., Schwingshackl, C., Séférian, R., Sutton, A. J., Sweeney, C., Tanhua, T., Tans, P. P., Tian, H., Tilbrook, B., Tubiello, F., van der Werf, G. R., Vuichard, N., Wada, C., Wanninkhof, R., Watson, A. J., Willis, D., Wiltshire, A. J., Yuan, W., Yue, C., Yue, X., Zaehle, S., and Zeng, J.: Global Carbon Budget 2021, Earth Syst. Sci. Data, 14, 1917–2005, https://doi.org/10.5194/essd-14-1917-2022, 2022.

Gray, A. R., Johnson, K. S., Bushinsky, S. M., Riser, S. C., Russell, J. L., Talley, L. D., Wanninkhof, R., Williams, N. L., and Sarmiento, J. L.: Autonomous biogeochemical floats detect significant carbon dioxide outgassing in the high-latitude Southern Ocean, Geophys. Res. Lett., 45(17), 9049–9057, https://doi.org/10.1029/2018GL078013, 2018.

Gutiérrez-Loza, L., Nilsson, E., Wallin, M. B., Sahlée, E., and Rutgersson, A.: On physical mechanisms enhancing air–sea CO_2 exchange, Biogeosciences, 19, 5645–5665, https://doi.org/10.5194/bg-19-5645-2022, 2022.

Hajima, T., Watanabe, M., Yamamoto, A., Tatebe, H., Noguchi, M. A.,

Abe, M., Ohgaito, R., Ito, A., Yamazaki, D., Okajima, H., Ito, A., Takata, K., Ogochi, K., Watanabe, S., and Kawamiya, M.: Development of the MIROC-ES2L Earth system model and the evaluation of biogeochemical processes and feedbacks, Geosci. Model Dev., 13, 2197–2244, https://doi.org/10.5194/gmd-13-2197-2020, 2020.

Heimdal, T. H., McKinley, G. A., Sutton, A. J., Fay, A. R., and Gloege, L.: Assessing improvements in global ocean pCO_2 machine learning reconstructions with Southern Ocean autonomous sampling, Biogeosciences, 21, 2159–2176, https://doi.org/10.5194/bg-21-2159-2024, 2024.

Honkanen, M., Tuovinen, J.-P., Laurila, T., Mäkelä, T., Hatakka, J., Kielosto, S., and Laakso, L.: Measuring turbulent CO_2 fluxes with a closed-path gas analyzer in a marine environment, Atmos. Meas. Tech., 11, 5335–5350, https://doi.org/10.5194/amt-11-5335-2018, 2018.

Hurrell, J. W., Holland, M. M., Gent, P. R., Ghan, S., Kay, J. E., Kushner, P. J., Lamarque, J.-F., Large, W. G., Lawrence, D., Lindsay, K., Lipscomb, W. H., Long, M. C., Mahowald, N., Marsh, D. R., Neale, R. B., Rasch, P., Vavrus, S., Vertenstein, M., Bader, D., Collins, W. D., Hack, J. J., Kiehl, J., and Marshall, S.: The Community Earth System Model: A framework for collaborative research, Bull. Amer. Meteor. Soc., 94, 1339–1360, https://doi.org/10.1175/BAMS-D-12-00121.1, 2013.

Jacobson, A. R., Gruber, N., Sarmiento, J. L., Gloor, M. and Fletcher, S. E. M.: A joint atmosphere-ocean inversion for surface fluxes of carbon dioxide: I. methods and global-scale fluxes, Global. Biogeochem. Cy., 21, GB1020, https://doi.org/10.1029/2005GB002556, 2007.

Jacobson, A. R., Schuldt, K. N., Tans, P., Arlyn Andrews, Miller, J. B., Oda, T., Mund, J., Weir, B., Ott, L., Aalto, T., Abshire, J. B., Aikin, K., Aoki, S., Apadula, F., Arnold, S., Baier, B., Bartyzel, J., Beyersdorf, A., Biermann, T., Biraud, S. C., Boenisch, H., Brailsford, G., Brand, W. A., Chen, G., Huilin Chen, Lukasz Chmura, Clark, S., Colomb, A., Commane, R., Conil, S., Couret, C., Cox, A., Cristofanelli, P., Cuevas, E., Curcoll, R., Daube, B., Davis, K. J., Wekker, S. de, Della Coletta, J., Delmotte, M., DiGangi, E., DiGangi, J. P., Di Sarra, A. G., Dlugokencky, E., Elkins, J. W., Emmenegger, L., Shuangxi Fang, Fischer, M. L., Forster, G., Frumau, A., Galkowski, M., Gatti, L. V., Gehrlein, T., Gerbig, C., Francois Gheusi, Gloor, E., Gomez-Trueba, V., Goto, D., Griffis, T., Hammer, S., Hanson, C., Haszpra, L., Hatakka, J., Heimann, M., Heliasz, M., Hensen, A., Hermansen, O., Hintsa, E., Holst, J., Ivakhov, V., Jaffe, D. A., Jordan, A., Joubert, W., Karion, A., Kawa, S. R., Kazan, V., Keeling, R. F., Keronen, P., Kneuer, T., Kolari, P., Kateřina Komínková, Kort, E., Kozlova, E., Krummel, P., Kubistin, D., Labuschagne, C., Lam, D. H., Lan, X., Langenfelds, R. L., Laurent,

O., Laurila, T., Lauvaux, T., Lavric, J., Law, B. E., Lee, J., Lee, O. S., Lehner, I., Lehtinen, K., Leppert, R., Leskinen, A., Leuenberger, M., Levin, I., Levula, J., Lin, J., Lindauer, M., Loh, Z., Lopez, M., Luijkx, I. T., Lunder, C. R., Machida, T., Mammarella, I., Manca, G., Manning, A., Manning, A., Marek, M. V., Martin, M. Y., Matsueda, H., McKain, K., Meijer, H., Meinhardt, F., Merchant, L., N. Mihalopoulos, Miles, N. L., Miller, C. E., Mitchell, L., Mölder, M., Montzka, S., Moore, F., Moossen, H., Morgan, E., Josep-Anton Morgui, Morimoto, S., Müller-Williams, J., J. William Munger, Munro, D., Myhre, C. L., Shin-Ichiro Nakaoka, Jaroslaw Necki, Newman, S., Nichol, S., Niwa, Y., Obersteiner, F., O'Doherty, S., Paplawsky, B., Peischl, J., Peltola, O., Piacentino, S., Jean-Marc Pichon, Pickers, P., Piper, S., Pitt, J., Plass-Dülmer, C., Platt, S. M., Prinzivalli, S., Ramonet, M., Ramos, R., Reyes-Sanchez, E., Richardson, S. J., Riris, H., Rivas, P. P., Ryerson, T., Saito, K., Sargent, M., Sasakawa, M., Scheeren, B., Schuck, T., Schumacher, M., Seifert, T., Sha, M. K., Shepson, P., Shook, M., Sloop, C. D., Smith, P., Stanley, K., Steinbacher, M., Stephens, B., Sweeney, C., Thoning, K., Timas, H., Torn, M., Tørseth, K., Trisolino, P., Turnbull, J., van den Bulk, P., van Dinther, D., Vermeulen, A., Viner, B., Vitkova, G., Walker, S., Watson, A., Wofsy, S. C., Worsey, J., Worthy, D., Dickon Young, Zaehle, S., Zahn, A., and Zimnoch, M.: CarbonTracker CT2022, Model published by NOAA Global Monitoring Laboratory, https://doi.org/10.25925/z1gj-3254 (last access: 20 May 2026), 2023.

Jin, C. X., Zhou, T. J., Chen, X. L., and Wu, B: Seasonally evolving dominant interannual variability mode of air–sea CO_2 flux over the western North Pacific simulated by CESM1-BGC, Sci. China Earth Sci. 60, 1854–1865, https://doi.org/10.1007/s11430-015-9085-4, 2017.

Johansson, M. M., Björkqvist, J.-V., Särkkä, J., Leijala, U., and Kahma, K. K.: Correlation of wind waves and sea level variations on the coast of the seasonally ice-covered Gulf of Finland, Nat. Hazards Earth Syst. Sci., 22, 813–829, https://doi.org/10.5194/nhess-22-813-2022, 2022.

Koseki, S., Tjiputra, J., Fransner, F., Crespo, L. R., and Keenlyside, N. S.: isentangling the impact of Atlantic Niño on sea–air CO_2 flux. Nat. Commun. 14, 3649, https://doi.org/10.1038/s41467-023-38718-9, 2023.

Krall, K. E., Smith, A. W., Takagaki, N., and Jähne, B.: Air–sea gas exchange at wind speeds up to 85 m s^{-1}, Ocean Sci., 15, 1783–1799, https://doi.org/10.5194/os-15-1783-2019, 2019.

Lan, Y.-Y., Hsu, H.-H., Tsuang, B.-J., and Tu, C.-Y.: rceclccr/CAM5_SIT_v1.0 (v1.0.0), Zenodo [code], https://doi.org/10.5281/zenodo.5510795, 2021.

Lan, Y.-Y.: POP2–waves coupled model in CESM1.2.2 framework,

Zenodo [code], https://doi.org/10.5281/zenodo.15795234, 2025.

Li, S, Babanin, A. V., and Guan, C.: Dimensionless Parameterizations of Air–Sea CO_2 Gas Transfer Velocity on Surface Waves, Tellus B: Chem. Phys. Meteorol., 75(1), 1–12, https://doi.org/10.16993/tellusb.1867, 2023.

Liu, B., Six, K. D., and Ilyina, T.: Incorporating the stable carbon isotope 13C in the ocean biogeochemical component of the Max Planck Institute Earth System Model, Biogeosciences, 18, 4389–4429, https://doi.org/10.5194/bg-18-4389-2021, 2021.

Long, M. C., Lindsay, K., Peacock, S., Moore, J. K., and Doney, S. C.: Twentieth-Century oceanic carbon uptake and storage in CESM1 (BGC), J. Climate, 26, 6775–6800, https://doi.org/10.1175/JCLI-D-12-00184.1, 2013.

Long, M. C., Moore, J. K., Lindsay, K., Levy, M., Doney, S. C., Luo, J. Krumhardt, K. M., Letscher, R. T., Grover, M., and Sylvester, T.: Simulations with the marine biogeochemistry library (MARBL). J. Adv. Model. Earth Sy., 13(12), e2021MS002647. https://doi.org/10.1029/2021MS002647, 2021.

Lovato, T., Peano, D., Butenschön, M., Materia, S., Iovino, D., Scoccimarro, E., Fogli, P. G., Cherchi, A., Bellucci, A., Gualdi, S., Masina, S., and Navarra, A.: CMIP6 Simulations With the CMCC Earth System Model (CMCC-ESM2), J. Adv. Model. Earth Sy., 14, e2021MS002814, https://doi.org/10.1029/2021MS002814, 2022.

Lovenduski, N. S., Yeager, S. G., Lindsay, K., and Long, M. C.: Predicting near-term variability in ocean carbon uptake, Earth Syst. Dynam., 10, 45–57, https://doi.org/10.5194/esd-10-45-2019, 2019.

Macovei, V. A., Petersen, W., Brix, H., and Voynova, Y. G.: Reduced ocean carbon sink in the south and central North Sea (2014–2018) revealed from FerryBox observations Geophys. Res. Lett., 48, e2021GL092645, https://doi.org/10.1029/2021GL092645, 2021.

Mauritsen, T., Bader, J., Becker, T., Behrens, J., Bittner, M., Brokopf, R., Brovkin, V., Claussen, M., Crueger, T., Esch, M., Fast, I., Fiedler, S., Flaeschner, D., Gayler, V., Giorgetta, M., Goll, D. S., Haak, H., Hagemann, S., Hedemann, C., Hohenegger, C., Ilyina, T., Jahns, T., Jimenéz-de-la Cuesta, D., Jungclaus, J., Kleinen, T., Kloster, S., Kracher, D., Kinne, S., Kleberg, D., Lasslop, G., Kornblueh, L., Marotzke, J., Matei, D., Meraner, K., Mikolajewicz, U., Modali, K., Moebis, B., Mueller, W. A., Nabel, J. E. M. S., Nam, C. C. W., Notz, D., Nyawira, S.-S., Paulsen, H., Peters, K., Pincus, R., Pohlmann, H., Pongratz, J., Popp, M., Raddatz, T. J., Rast, S., Redler, R., Reick, C. H., Rohrschneider, T., Schemann, V., Schmidt, H., Schnur, R., Schulzweida, U., Six, K. D., Stein, L., Stemmler, I., Stevens, B., von Storch, J.-S., Tian, F., Voigt, A., Vrese, P., Wieners, K.-H., Wilkenskjeld, S., Winkler, A., and Roeckner, E.: Developments in the MPI-M Earth System Model version 1.2 (MPI-

ESM1.2) and Its Response to Increasing CO_2, J. Adv. Model. Earth Sy., 11, 998–1038, https://doi.org/10.1029/2018MS001400, 2019.

McKinley, G. A., Fay, A. R., Eddebbar, Y. A., Gloege, L., and Lovenduski, N. S.: External forcing explains recentdecadal variability of the ocean carbonsink, AGU Advances, 1,e2019AV00014, https://doi.org/10.1029/2019AV000149, 2020.

Mellor, G. L., Donelan, M. A., and Oey, L.-Y.: A surface wave model for coupling with numerical ocean circulation models. J. Atmos. Ocean. Technol., 25(10), 1785–1807, https://doi.org/10.1175/2008JTECHO573.1, 2008.

Monahan, E. C., and Spillane, M. C.: The role of oceanic whitecaps in air–sea gas exchange, in: Gas transfer at water surfaces, edited by: Brutsaert, W. and Jirka, G. H., Reidel, Hingham, MA, 495–503, https://doi.org/10.1007/978-94-017-1660-4_45, 1984.

Moore, J. K., Lindsay, K., Doney, S. C., Long, M. C., and Misumi, K.: Marine ecosystem dynamics and biogeochemical cycling in the Community Earth System Model [CESM1 (BGC)]: Comparison of the 1990s with the 2090s under the RCP4. 5 and RCP8. 5 scenarios, J. Climate, 26, 9291–9312, https://doi.org/10.1175/JCLI-D-12-00566.1, 2013.

Müller, J. D., Gruber, N., Carter, B., Feely, R., Ishii, M., Lange, N., Lauvset, S. K., Murata, A., Olsen, A., Pérez, F. F., Sabine, C., Tanhua, T., Wanninkhof, R., and Zhu, D.: Decadal trends in the oceanic storage of anthropogenic carbon from 1994 to 2014. AGU Advances, 4, e2023AV000875, https://doi.org/10.1029/2023AV000875, 2023.

Reichl, B. G., and Deike, L.: Contribution of Sea-State Dependent Bubbles to Air–sea Carbon Dioxide Fluxes, Geophys. Res. Lett., 47, e2020GL087267. https://doi.org/10.1029/2020GL087267, 2020.

Roobaert, A., Resplandy, L., Laruelle, G. G., Liao, E., and Regnier, P.: Unraveling the physical and biological controls of the global coastal CO_2 sink, Global Biogeochem. Cy., 38, e2023GB007799. https://doi.org/10.1029/2023GB007799, 2024.

Rustogi, P., Resplandy, L., Liao, E., Reichl, B. G., and Deike, L.: Influence of wave-induced variability on ocean carbon uptake. Global Biogeochem. Cy., 39, e2024GB008382. https://doi.org/10.1029/2024GB008382, 2025.

Sabine, C., Sutton, A., McCabe, K., Lawrence-Slavas, N., Alin, S, Feely, R., Jenkins, R., Maenner, S., Meinig, C., Thomas, J., van Ooijen, E., Passmore, A., and Tilbrook, B.: Evaluation of a new carbon dioxide system for autonomous surface vehicles, J. Atmos. Oceaen. Tech., 37, 1305–1317, https://doi.org/10.1175/JTECH-D-20-0010.1, 2020.

Séférian, R., Nabat, P., Michou, M., Saint-Martin, D., Voldoire, A., Colin, J., Decharme, B., Delire, C., Berthet, S., Chevallier, M.,

Sénési, S., Franchisteguy, L., Vial, J., Mallet, M., Joetzjer, E., Geoffroy, O., Guérémy, J.-F., Moine, M.-P., Msadek, R., Ribes, A., Rocher, M., Roehrig, R., Salas-y-Mélia, D., Sanchez, E., Terray, L., Valcke, S., Waldman, R., Aumont, O., Bopp, L., Deshayes, J., Éthé, C., and Madec, G.: Evaluation of CNRM Earth-System model, CNRM-ESM2-1: role of Earth system processes in present-day and future climate, J. Adv. Model. Earth Sy., 11, 4182–4227, https://doi.org/10.1029/2019MS001791, 2019.

Séférian, R., Berthet, S., SGO, Y., Bopp, L., Gehlen, M., and Joos, F.: Assessment of ocean carbon cycle models in the JULES-OM2 configurations, Geosci. Model Dev., 13, 4521–4543, https://doi.org/10.5194/gmd-13-4521-2020, 2020.

Seland, Ø., Bentsen, M., Olivié, D., Toniazzo, T., Gjermundsen, A., Graff, L. S., Debernard, J. B., Gupta, A. K., He, Y.-C., Kirkevåg, A., Schwinger, J., Tjiputra, J., Aas, K. S., Bethke, I., Fan, Y., Griesfeller, J., Grini, A., Guo, C., Ilicak, M., Karset, I. H. H., Landgren, O., Liakka, J., Moseid, K. O., Nummelin, A., Spensberger, C., Tang, H., Zhang, Z., Heinze, C., Iversen, T., and Schulz, M.: Overview of the Norwegian Earth System Model (NorESM2) and key climate response of CMIP6 DECK, historical, and scenario simulations, Geosci. Model Dev., 13, 6165–6200, https://doi.org/10.5194/gmd-13-6165-2020, 2020.

Shutler, J. D., Wanninkhof, R., Nightingale, P. D., Woolf, D. K., Bakker, D. C., Watson, A., Ashton, I., Holding, T., Chapron, B., Quilfen, Y., Fairall, C., Schuster, U., Nakajima, M., and Donlon, C. J.: Satellites will address critical science priorities for quantifying ocean carbon, Front. Ecol. Environ., 18(1): 27–35, http://dx.doi.org/10.1002/fee.2129, 2019.

Sigmond, M., Anstey, J., Arora, V., Digby, R., Gillett, N., Kharin, V., Merryfield, W., Reader, C., Scinocca, J., Swart, N., Virgin, J., Abraham, C., Cole, J., Lambert, N., Lee, W.-S., Liang, Y., Malinina, E., Rieger, L., von Salzen, K., Seiler, C., Seinen, C., Shao, A., Sospedra-Alfonso, R., Wang, L., and Yang, D.: Improvements in the Canadian Earth System Model (CanESM) through systematic model analysis: CanESM5.0 and CanESM5.1, Geosci. Model Dev., 16, 6553–6591, https://doi.org/10.5194/gmd-16-6553-2023, 2023.

Signorini, S. R., and McClain, C. R.: Effect of uncertainties in climatologic wind, ocean pCO_2, and gas transfer algorithms on the estimate of global sea–air CO_2 flux, Global Biogeochem. Cy., 23, GB2025, https://doi.org/10.1029/2008GB003246, 2009.

Smith, R., Jones, P., Briegleb, B., Bryan, F., Danabasoglu, G., Dennis, J., Dukowicz, J., Eden, C., Fox-Kemper, B., Gent, P., Hecht, M., Jayne, S., Jochum, M., Large, W., Lindsay, K., Maltrud, M., Norton, N., Peacock, S., Vertenstein, M., and Yeager, S.: The Parallel Ocean Program (POP) reference manual ocean component of the Community Climate System Model (CCSM) and Community Earth

System Model (CESM), Los Alamos National Laboratory Tech. Rep. LAUR-10-01853, 140 pp, https://www2.cesm.ucar.edu/models/cesm1.0/pop2/doc/sci/POPRefManual.pdf, 2010.

Soloviev, A., and Lukas, R.: Effects of Bubbles and Sea Spray on Air–Sea Exchange in Hurricane Conditions, Bound.-Layer Meteorol., 136, 365–376, https://doi.org/10.1007/s10546-010-9505-0, 2010.

Stock, C. A., Dunne, J. P., Fan, S., Ginoux, P., John, J., Krasting, J. P., Laufkötter, C., Paulot, F., and Zadeh, N.: Ocean biogeochemistry in GFDL's Earth System Model 4.1 and its response to increasing atmospheric CO_2, J. Adv. Model. Earth Sy., 12, e2019MS002043, https://doi.org/10.1029/2019MS002043, 2020.

Sutton, A. J., Sabine, C. L., Maenner-Jones, S., Lawrence-Slavas, N., Meinig, C., Feely, R. A., Mathis, J. T., Musielewicz, S., Bott, R., McLain, P. D., Fought, H. J., and Kozyr, A.: A high-frequency atmospheric and seawater pCO_2 data set from 14 open-ocean sites using a moored autonomous system, Earth Syst. Sci. Data, 6, 353–366, https://doi.org/10.5194/essd-6-353-2014, 2014.

Tjiputra, J. F., Schwinger, J., Bentsen, M., Morée, A. L., Gao, S., Bethke, I., Heinze, C., Goris, N., Gupta, A., He, Y.-C., Olivié, D., Seland, Ø., and Schulz, M.: Ocean biogeochemistry in the Norwegian Earth System Model version 2 (NorESM2), Geosci. Model Dev., 13, 2393–2431, https://doi.org/10.5194/gmd-13-2393-2020, 2020.

Tokoro, T., Hosokawa, S., Miyoshi, E., Tada, K., Watanabe, K., Montani, S., Kayanne, H., and Kuwae, T.: Net uptake of atmospheric CO_2 by coastal submerged aquatic vegetation, Glob. Change Biol., 20, 1873–1884, https://doi.org/10.1111/gcb.12543, 2014.

Van Dam, B., Polsenaere, P., Barreras-Apodaca, A., Lopes, C., Sanchez-Mejia, Z., Tokoro, T., Kuwae, T., Loza, L. G., Rutgersson, A., Fourqurean, J., and Thomas, H.: Global trends in air-water CO_2 exchange over seagrass meadows revealed by atmospheric Eddy Covariance, Global Biogeochem. Cy., 35, e2020GB006848, https://doi.org/10.1029/2020GB006848, 2021.

Wanninkhof, R.: Relationship between wind speed and gas exchange over the ocean, J. Geophys. Res., 97(C5), 7373–7382. https://doi.org/10.1029/92JC00188, 1992.

Wanninkhof, R.: Relationship between wind speed and gas exchange over the ocean revisited, Limnol. Oceanogr.: Methods, 12(6), 351–362. https://doi.org/10.4319/lom.2014.12.351, 2014.

Weiss, R. F.: Carbon dioxide in water and seawater: the solubility of a non-ideal gas, Mar. Chem., 2 (3), pp. 203-215, https://doi.org/10.1016/0304-4203(74)90015-2, 1974.

Williams, N. L., Juranek, L. W., Feely, R. A., Johnson, K. S., Sarmiento, J. L., Talley, L. D., Dickson, A. G., Gray, A. R., Wanninkhof, R.,

Russell, J. L., and Riser, S. C.: Calculating surface ocean pCO_2 from biogeochemical Argo floats equipped with pH: An uncertainty analysis, Global Biogeochem. Cy., 31, 591–604, https://doi.org/10.1002/2016GB005541, 2017.

Wu, Y., and Qi, D.: The controversial Southern Ocean air–sea CO_2 flux in the era of autonomous ocean observations, Sci. Bull., 68, 21, 2519-2522, https://doi.org/10.1016/j.scib.2023.08.059, 2023.

Wu, L., Cai, Y., and Rutgersson, A.: Ocean surface waves impact on global air–sea CO_2 flux, Biogeochem., 168, 68, https://doi.org/10.1007/s10533-025-01267-y, 2025.

Yang, X., Wynn-Edwards, C. A., Strutton, P. G., and Shadwick, E. H.: Drivers of air–sea CO_2 flux in the subantarctic zone revealed by time series observations. Global Biogeochem. Cy., 38, e2023GB007766, https://doi.org/10.1029/2023GB007766, 2024.

Yool, A., Palmiéri, J., Jones, C. G., de Mora, L., Kuhlbrodt, T., Popova, E. E., Nurser, A. J. G., Hirschi, J., Blaker, A. T., Coward, A. C., Blockley, E. W., and Sellar, A. A.: Evaluating the physical and biogeochemical state of the global ocean component of UKESM1 in CMIP6 historical simulations, Geosci. Model Dev., 14, 3437–3472, https://doi.org/10.5194/gmd-14-3437-2021, 2021.

Zhou, X., Reichl, B. G., Romero, L., and Deike, L.: A sea state dependent gas transfer velocity for CO_2 unifying theory, model, and field data, Earth Space Sci., 10, e2023EA003237, https://doi.org/10.1029/2023EA003237, 2023.

Ziehn, T., Chamberlain, M., Law, R., Lenton, A., Bodman, R., Dix, M., Stevens, L., Wang, Y.-P., and Srbinovsky, J.: The Australian Earth System Model: ACCESS-ESM1.5, J. South. Hemisph. Earth Syst. Sci., 70(1) 193-214, https://doi.org/10.1071/ES19035, 2020.

Table 1. Characteristics of the 12 key regions exhibiting prominent air–sea CO_2 flux variability across the three major ocean basins.

Basins	Key regions
the Pacific Ocean	the Northwestern Pacific (NWP), Eastern Equatorial Pacific (EEP), Northeastern Pacific (NEP), South Pacific Ocean 1 (SPO1), and South Pacific Ocean 2 (SPO2)
the Indian Ocean	the North Indian Ocean (NIO), South Indian Ocean 1 (SIO1), and South Indian Ocean 2 (SIO2)
the Atlantic Ocean	the North Atlantic Ocean 1 (NAO1), North Atlantic Ocean 2 (NAO2), Equatorial Atlantic Ocean (EAO), and South Atlantic Ocean (SAO)

Table 2. Intercomparison of Earth System Model for estimating air–sea CO_2 flux

Earth System Model	Ocean components	Wave-informed air–sea CO_2 flux	$k_{w,660}$ parameterization	Reference
CESM1[1]	POP2[2]	no	U_{10} (Wannikhof 1992)	Chikamoto and DiNezio, 2021; Chikamoto et al., 2023
CESM2[3]	POP2[2]	no	U_{10} (Wannikhof 2014)	Danabasoglu et al., 2020
NorESM2[4]	BLOM[5]	no	U_{10} (Wannikhof 2014)	Seland et al., 2020; Tjiputra et al., 2020
MPI-ESM1.2[6]	MPIOM 1.6[7]	no	U_{10} (Wannikhof 2014)	Mauritsen et al., 2019; Liu et al., 2021
ACCESS-ESM1.5[8]	MOM5[9]	no	U_{10} (Wannikhof 1992)	Ziehn et al., 2020
CMCC-ESM2[10]	NEMO v3.6[11]	no	U_{10} (Wannikhof 1992)	Lovato et al., 2022
CanESM5[12]	CanNEMO[13]	no	U_{10} (Wannikhof 1992)	Sigmond et al., 2023
GFDL-ESM4.1[14]	MOM6[15]	no	U_{10} (Wannikhof 2014)	Stock et al., 2020; Roobaert et al., 2024
IPSL-CM6A-LR[16]	NEMO-PISCES[17]	no	U_{10} (Wannikhof 1992)	Boucher et al., 2020
MIROC-ES2L[18]	COCO 4.0[19]	no	U_{10} (Wannikhof 1992)	Hajima et al., 2020
UKESM1[20]	NEMO v3.6[11]	no	U_{10} (Wannikhof 1992)	Yool et al., 2021
CNRM-ESM2-1[21]	NEMO-PISCES[17]	no	U_{10} (Wannikhof 1992)	Séférian et al., 2019
-[22]	NEMO-PISCES[17]	Yes	H_s, u^* (Deike and Melville, 2018)	Wu et al., 2025
-[22]	MOM6-COBALTv2[23]	Yes	H_s, u^* (Deike and Melville, 2018)	Rustogi et al., 2025
CESM1-POP2–waves[24]	POP2–waves coupled model	Yes	H_s, u^* (Deike and Melville, 2018)	This study

Note:

[1]CESM1: the Community Earth System Model version 1 of the National Center for Atmospheric Research (NCAR);

[2]POP2: the Parallel Ocean Program version 2 of NCAR;

[3]CESM2: CESM version 2;

[4]NorESM2: The Norwegian Earth System Model version 2;

[5]BLOM: Bergen Layered Ocean Model;

[6]MPI-ESM1.2: the Max Planck Institute for Meteorology Earth System Model version 1.2;

[7]MPIOM 1.6: the Max-Planck Institute Ocean Model version 1.6;

[8]ACCESS-ESM1.5: the Australian Community Climate and Earth System Simulator form an Earth System Model version 1.5;

[9]MOM5: the GFDL Modular Ocean Model version 5;

[10]CMCC-ESM2: the Euro-Mediterranean Centre on Climate Change (CMCC) Earth System Model version 2;

[11]NEMO v3.6: Nucleus for European Modelling of the Ocean version 3.6;

[12]CanESM5: the Canadian Earth System Model version 5;

[13]CanNEMO: NEMO version 3.4 modified for CanESM;

[14]GFDL-ESM4.1: the Geophysical Fluid Dynamics Laboratory's Earth System Model 4.1;

[15]MOM6: the GFDL Modular Ocean Model version 6;

[16]IPSL-CM6A-LR : version 6 of the Institut Pierre-Simon Laplace (IPSL) climate model;

[17]NEMO-PISCES: Nucleus for European Modelling of the Ocean, Pelagic Interaction Scheme for Carbon and Ecosystem Studies ocean general circulation and biogeochemistry model;

[18]MIROC-ES2L: the Model for Interdisciplinary Research on Climate, Earth System version 2;

[19]COCO 4.0: CCSR (Center for Climate System Research) Ocean Component Model version 4.0:

[20]UKESM1: the U.K. Earth System Model;

[21]CNRM-ESM2-1: the Earth system (ES) model of second generation developed by the Centre National de Recherches Météorologiques (CNRM);

[22]The simulations were conducted using global ocean-only models rather than full Earth System Models.

[23]MOM6-COBALTv2: Geophysical Fluid Dynamics Laboratory global ocean model (Modular Ocean Model, MOM6) coupled with sea ice and biogeochemistry (Carbon, Ocean Biogeochemistry and Lower Trophics, COBALTv2);

[24]CESM1-POP2–waves: POP2–waves coupled model based on CESM1.

Table 3. Relative magnitudes of model–data biases (%), defined as the monthly mean absolute deviation normalized by the model's corresponding monthly variability range (95th minus 5th percentile)

Model	NWP	EEP	NEP	SPO1	NIO	SIO1	NAO1	EAO	SAO
POP2–waves	21.9	46.5	24.7	21.1	14.5	17.8	14.3	15.0	31.6
B–CTL (baseline)	26.8	71.5	25.3	22.1	16.2	21.9	15.4	11.9	36.0

Note:

Abbreviations: NWP: Northwestern Pacific; EEP: Eastern Equatorial Pacific; NEP: Northeastern Pacific; SPO1: South Pacific Ocean 1; NIO: North Indian Ocean; SIO1: South Indian Ocean 1; NAO1: North Atlantic Ocean 1; EAO: Equatorial Atlantic Ocean; SAO: South Atlantic Ocean.

The relative magnitude of model–data bias (%) across the 360-month period is defined and calculated as follows:

$$\text{Model} - \text{data biases (\%)} = \frac{1}{12}\sum_{i=1}^{12}\frac{|Mi - Oi|}{P_{95}(M) - P_5(M)}$$

where *M*i and *O*i represent the monthly mean values simulated by (POP2–waves or B–CTL) and reference (NOAA CT2022 inversion) air–sea CO_2 fluxes for the month mean of month i (i = 1, 2, …, 12), respectively. P_{95} (*M*) and P_5 (*M*) denote the 95th and 5th percentiles, respectively, of each calendar month's values over the 30-year period, representing the corresponding range of monthly variability in the model.

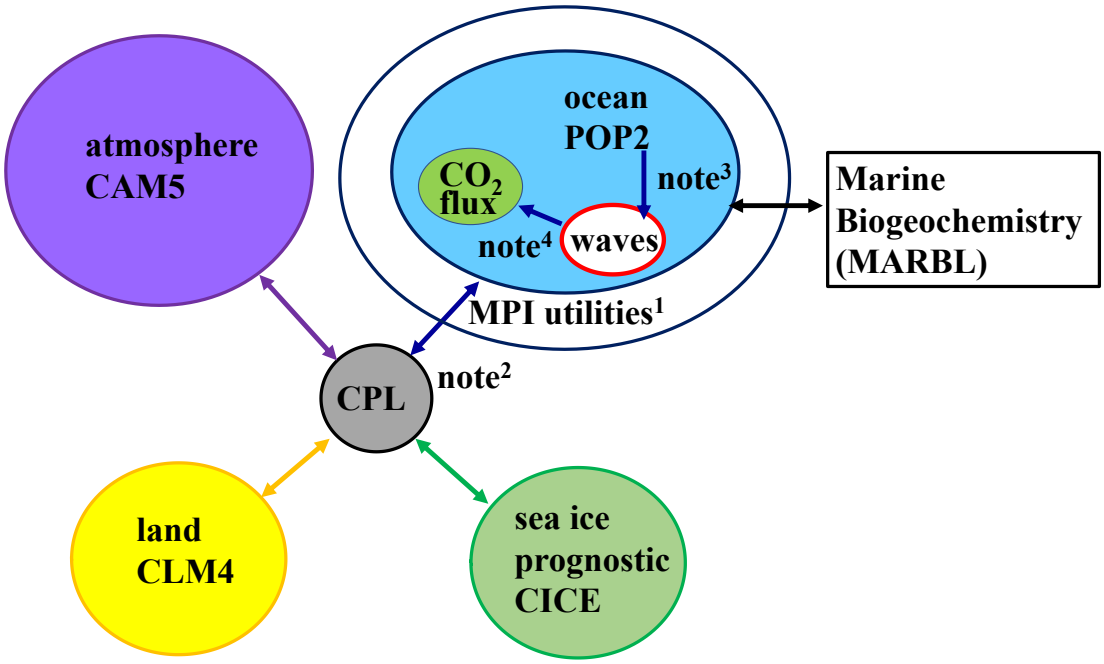

Figure 1. Architecture diagram for POP2–waves experiment in CESM1.2.2 framework, all components adhere to the CESM 1.2.2 framework, except for certain parts of the ocean component. The model components including components for the atmosphere [Community Atmosphere Model version 5 (CAM5)], land [Community Land Model version 4 (CLM4)], ocean [Parallel Ocean Program, version 2 (POP2)], along with its associated modules—the waves module (waves) and the Marine Biogeochemistry (MARBL) module—sea ice [prognostic Los Alamos Sea Ice Model (CICE)], and the coupler (CPL).

Note:

[1]The wave-module variables are communicated between neighboring blocks via MPI, including zonal and meridional 10-m winds, wave radiation stress, subsurface momentum, and wave radiation and energy densities.

[2]To transfer variables such as zonal and meridional 10-m winds and friction velocity (including sea surface and ice fraction) from the CPL to POP2.

[3]The wave module receives variables from POP2, including the interpolation of depth-varying currents from z-coordinates (60 levels) to the wave module's vertical sigma coordinates (21 levels), along with ocean grid information in the x, y, and z directions.

[4]The wave module outputs significant wave height and friction velocity from the CPL for calculating the bubble-mediated gas transfer velocity in Eq. (3).

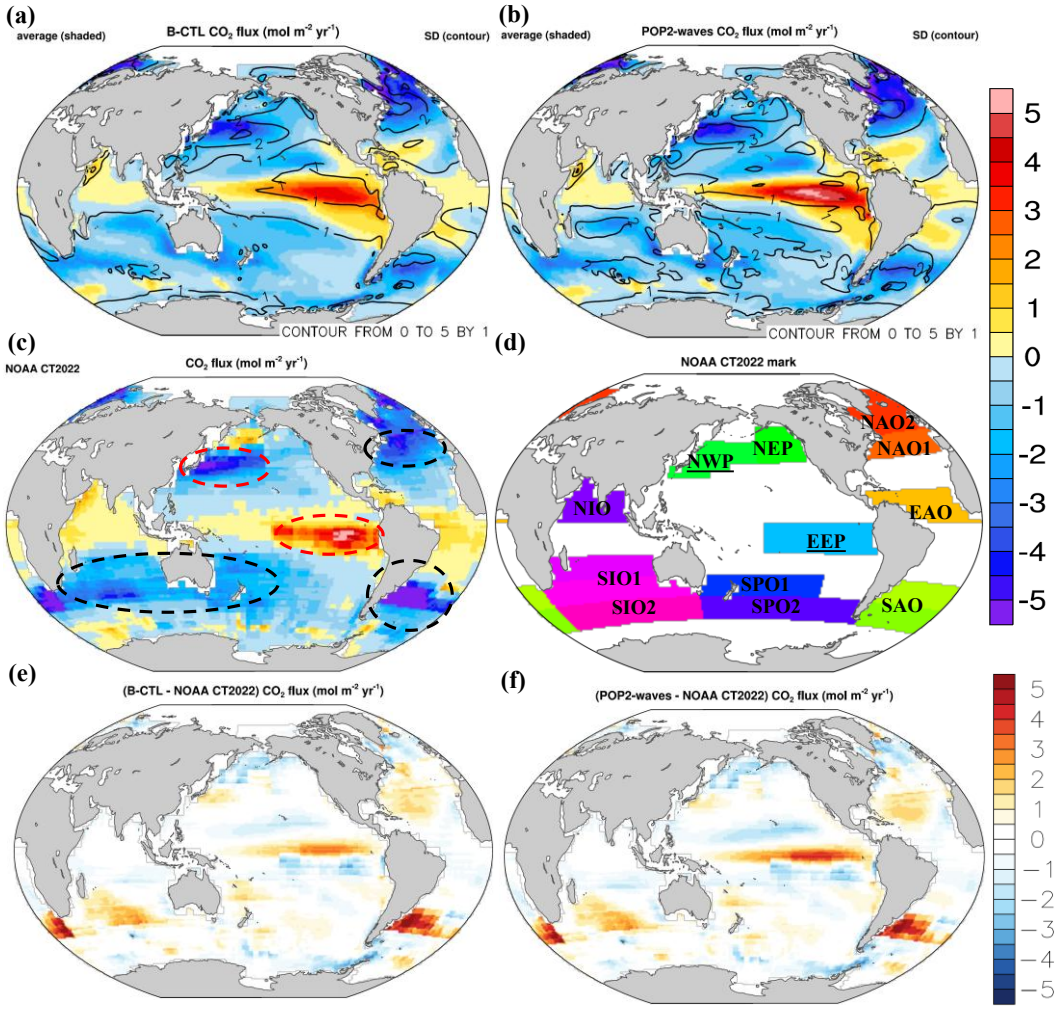

Figure 2. Climatological mean air–sea CO_2 flux (mol m^{-2} yr^{-1}; shaded) and monthly standard deviation (SD; contour): (a) B–CTL; (b) POP2–waves; (c) NOAA CT2022: red dashed lines highlight the primary oceanic CO_2 outgassing and uptake regions in the Pacific Ocean, while black dashed lines mark regions with an air–sea CO_2 flux below -2 mol m^{-2} yr^{-1}; (d) Based on NOAA CT2022, 12 key regions exhibiting significant air–sea CO_2 flux variability have been identified among the 30 ocean basins defined in the CT2022 model documentation (Jacobson et al., 2023) for optimizing flux inversions. These include: (1) Pacific Ocean: Northwestern Pacific (NWP), Eastern Equatorial Pacific (EEP) (underlined labels highlighted with red dashed lines in Fig. 2c), as well as Northeastern Pacific (NEP), South Pacific Ocean 1 (SPO1), and South Pacific Ocean 2 (SPO2); (2) Indian Ocean: North Indian Ocean (NIO), South Indian Ocean 1 (SIO1), and South Indian Ocean 2 (SIO2); (3) Atlantic Ocean: North Atlantic Ocean 1 (NAO1), North Atlantic Ocean 2 (NAO2), Equatorial Atlantic Ocean (EAO), and South Atlantic Ocean (SAO), (e) the air–sea CO_2 flux difference between B–CTL and NOAA CT2022, and (f) same as (e), but between POP2–waves and NOAA CT2022.

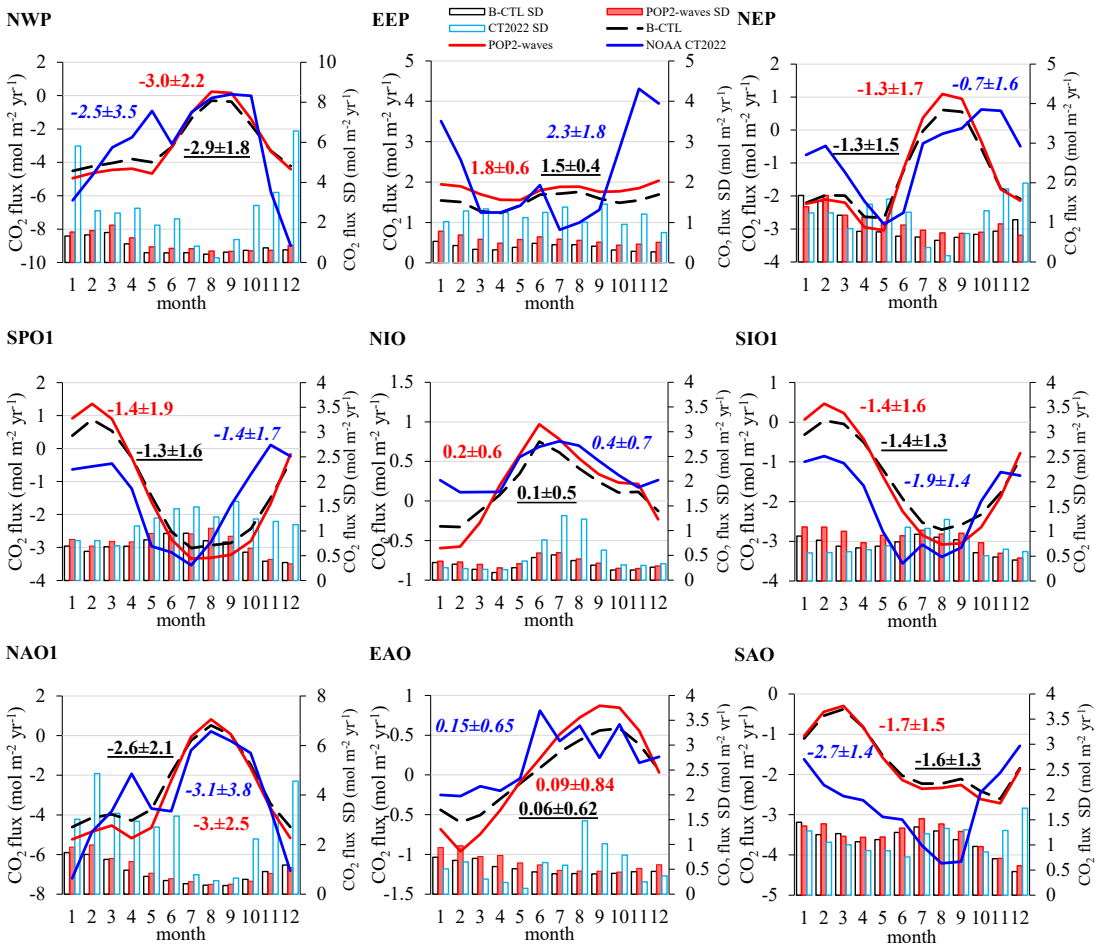

Figure 3. Climatological monthly mean CO_2 flux for nine highly correlated regions defined in Fig. 2d (NWP, EEP, NEP, SPO1, NIO, SIO1, NAO1, EAO, and SAO). Lines indicate values for B–CTL (black dashed), POP2–waves (red solid), and NOAA CT2022 (blue solid). Regional-average values are distinguished by a black underline for B–CTL, red font for POP2–waves, and blue italics for NOAA CT2022. Monthly standard deviation (SD) is shown as bars: black hollow (B–CTL), red solid (POP2–waves), and light blue hollow (NOAA CT2022).

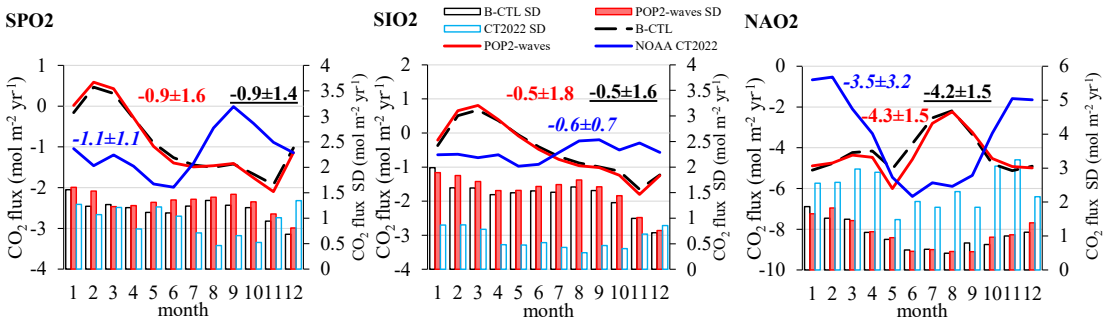

Figure 4. Same as Fig. 3, but for the low-correlation climatological average of the simulated CO_2 flux compared with NOAA CT2022, based on the three characteristic regions (SPO2, SIO2, and NAO2).

*Note: SPO2: South Pacific Ocean Region 2; SIO2: South Indian Ocean Region 2; NAO2: North Atlantic Ocean Region 2.

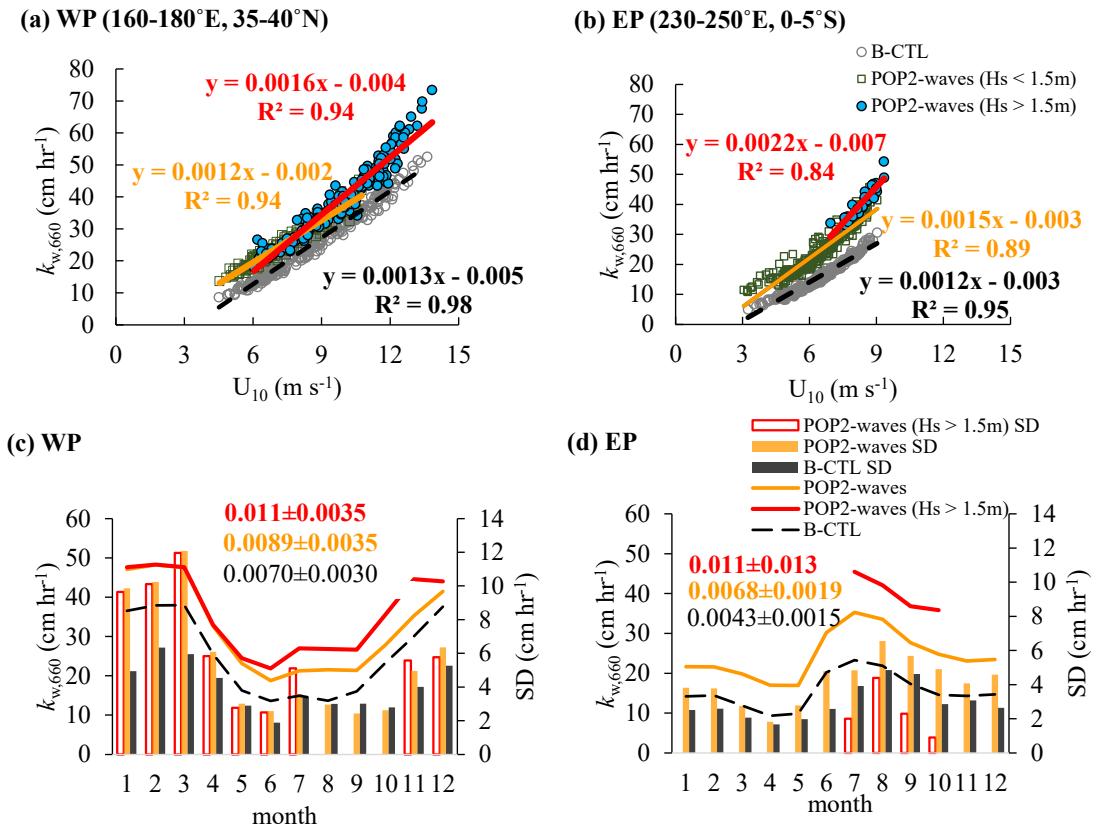

Figure 5. Scatter plots of monthly averaged gas transfer velocity ($k_{w,660}$) versus U_{10} for (a) the Western Pacific (WP; 160–180°E, 35–40°N) and (b) the Eastern Pacific (EP; 230–250°E, 0–5°S). Gray open circles, green open squares, and blue dots with black edges represent B–CTL, POP2–waves data for H_s < 1.5 m, and H_s > 1.5 m, respectively. Corresponding simple linear regressions (SLRs) and squared correlation coefficients (R^2) are shown with black dotted lines/text (B–CTL), orange solid lines/text (POP2–waves, H_s < 1.5 m), and red solid lines/text (POP2–waves, H_s > 1.5 m). Panels (c) and (d) display the monthly mean values of $k_{w,600}$ for WP and EP, respectively. Red and orange solid lines/text indicate POP2–waves (H_s > 1.5 m) and the average of all POP2–waves data, while the black dotted line/text represents B–CTL. The bar graph illustrates the standard deviation (SD) for each month over the WP and EP, red hollow bars for POP2–waves (H_s > 1.5 m), orange for average POP2–waves, and black for B–CTL.

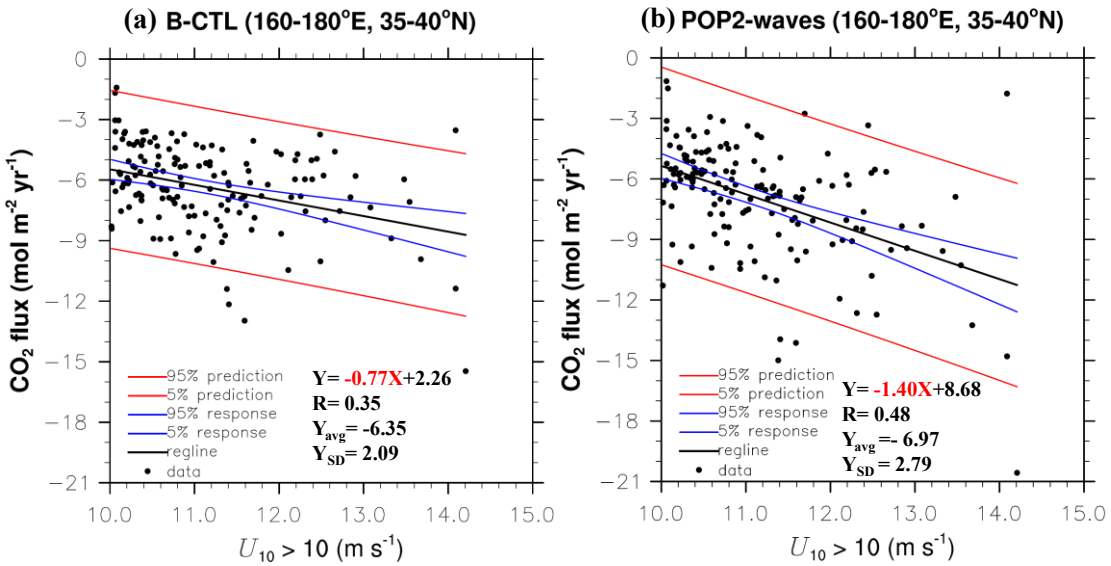

Figure 6. Scatter plots of air–sea CO_2 flux versus U_{10} with regression lines over the Western Pacific (160–180°E, 35–40°N) under high-wind conditions (U_{10} > 10 m s^{-1}) for (a) B–CTL and (b) POP2–waves experiments. Black dots indicate monthly mean values from each experiment. Blue lines denote the 95% and 5% confidence limits of the mean response, while red lines denote the 95% and 5% prediction intervals. The regression equation (Y = mx + b), correlation coefficient (R), mean CO_2 flux (Y_{avg}), and standard deviation (Y_{SD}) are shown to the right of the legend.

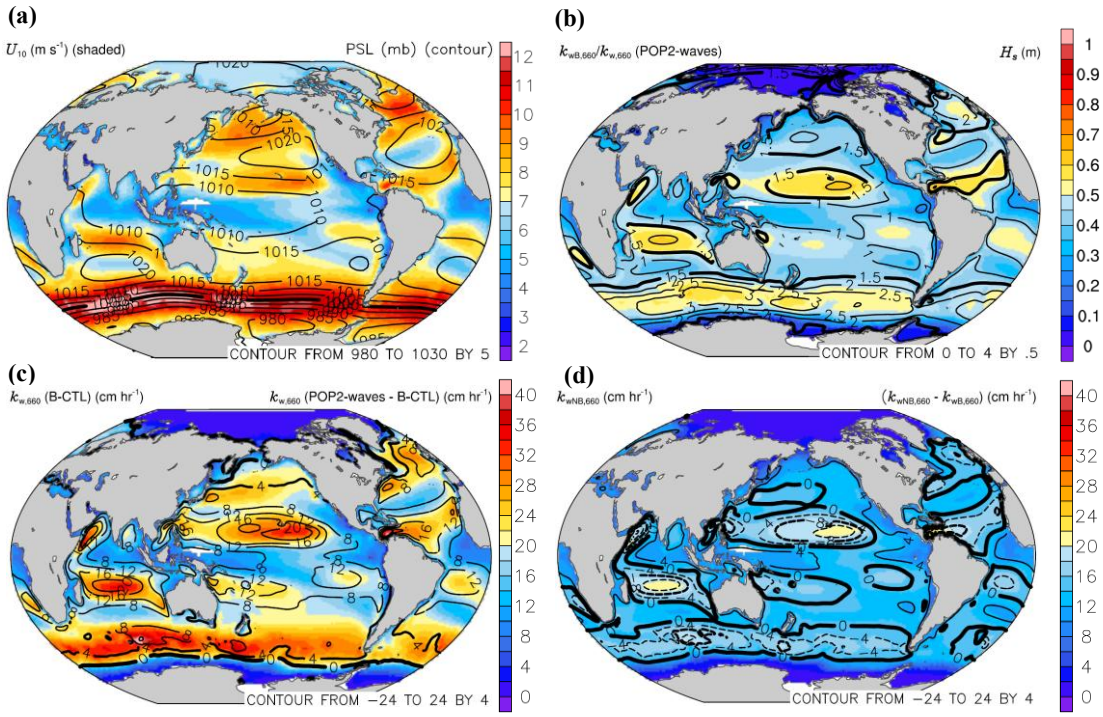

Figure 7. Effects of atmospheric factors and wave components on average gas transfer velocity: (a) Shaded areas represent 10-m wind speed (U_{10}, m s^{-1}) and contours show sea level pressure (PSL, mb); (b) color denotes the ratio of bubble-mediated ($k_{wB,660}$) to POP2–waves $k_{w,660}$ components, with contours representing significant wave height H_s (m) and thick lines marking H_s = 1.5m; (c) shading represents $k_{w,660}$ (B–CTL) and contours represent the difference $k_{w,660}$ (POP2–waves − B–CTL) in cm hr^{-1}; (d) shading shows the non-bubble-mediated component ($k_{wNB,660}$) and contours show the difference ($k_{wNB,660} - k_{wB,660}$) in cm hr^{-1}, with the thick contour lines at 0.

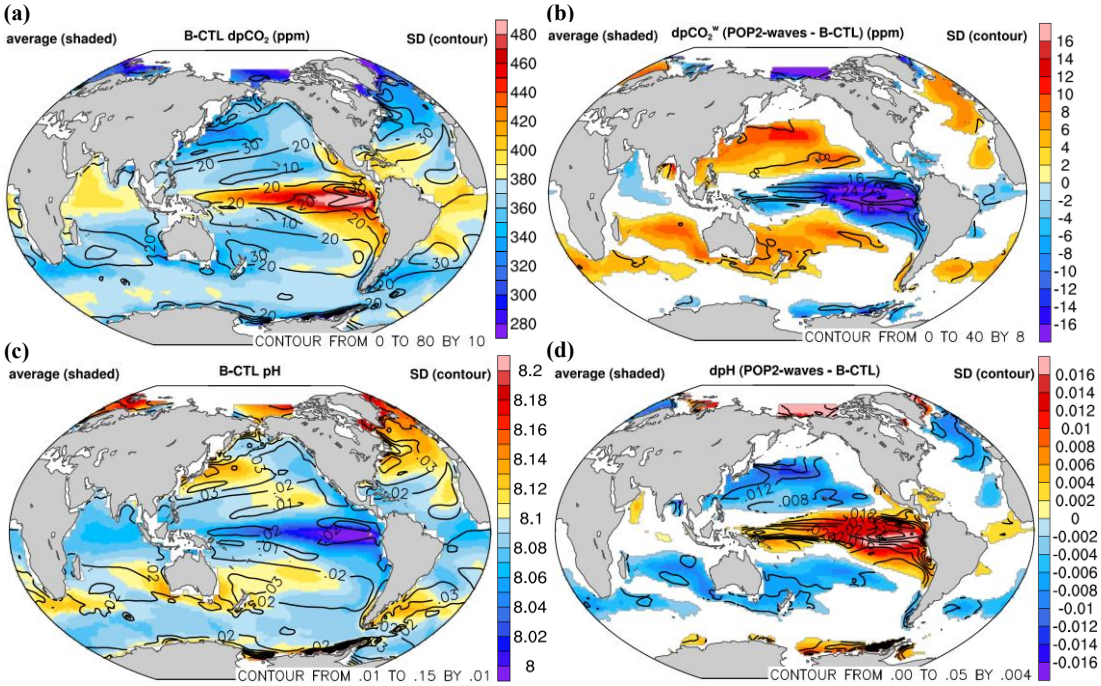

Figure 8. Spatial distributions of the 30-year climatological averages and model differences for $dpCO_2^w$ (ppm; panels a, b) and ocean surface pH (panels c, d). Climatological means are represented by shading, and their corresponding standard deviation (SD) is superimposed as contours. Panels (a) and (c) present baseline results from the B–CTL simulation. Panels (b) and (d) depict the structural differences between the POP2–waves and B–CTL experiments (POP2–waves minus B–CTL), where stippling indicates statistical significance at the 95% confidence level based on a Student's t-test.

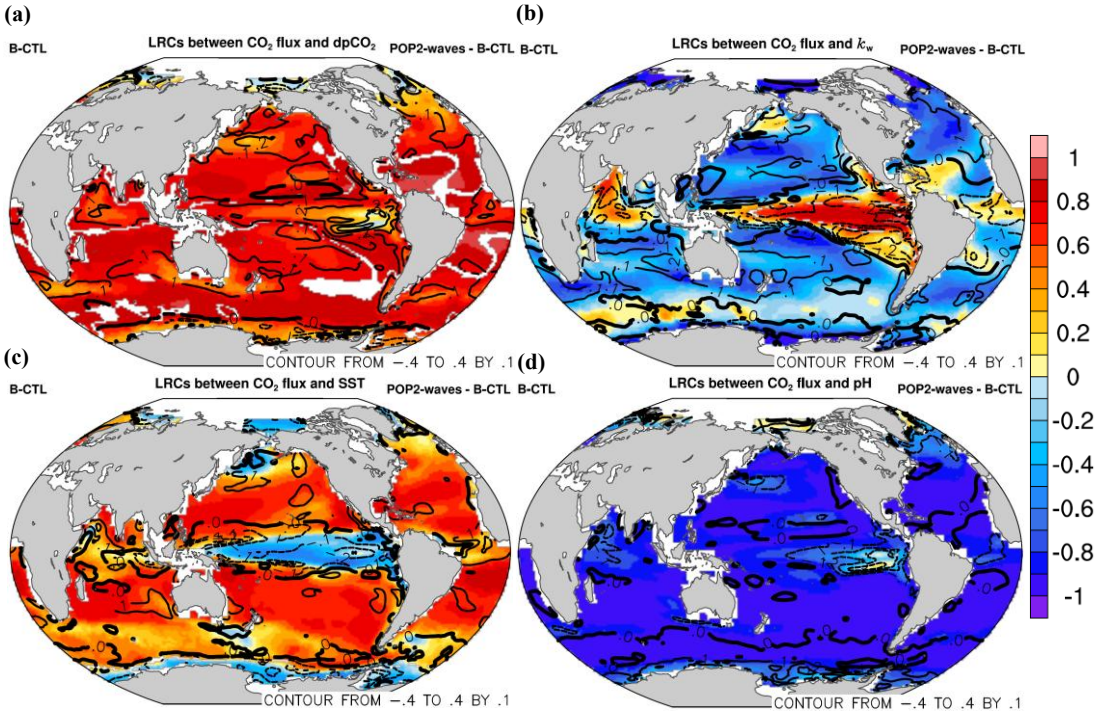

Figure 9. Spatial distributions of the 30-year averages of the linear regression coefficients (LRCs) between the CO_2 flux and (a) $dpCO_2$, ((b) $k_{w,660}$, (c) SST, and (d) pH. Shading represents the baseline LRCs from the B–CTL simulation, while overlaid contours depict the structural differences between the POP2–waves and B–CTL experiments (POP2–waves minus B–CTL). White areas denote regions where the LRCs are statistically insignificant at the 95% confidence level (based on a Student's t-test). All variables were standardized prior to the regression analysis.

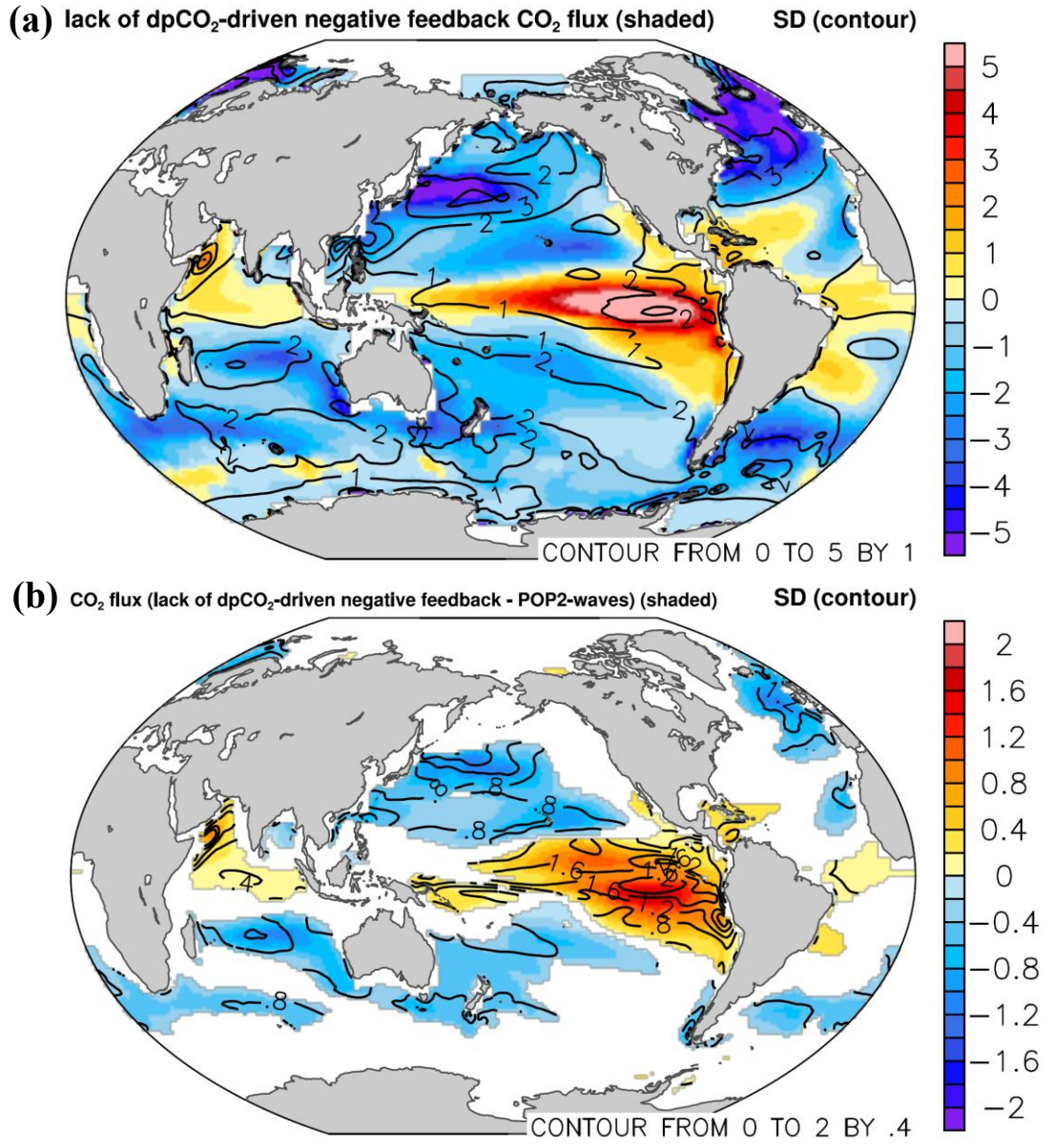

Figure 10. Estimated air–sea CO_2 flux assuming the absence of the $dpCO_2$-driven negative feedback mechanism. (a) Air–sea CO_2 flux calculated using uncoupled, independent $dpCO_2$ values from the B–CTL baseline and wave-dependent $k_{w,660}$ formulations (labeled as the "lack of $dpCO_2$-driven negative feedback" case). Shading represents the climatological mean, and contours indicate the corresponding standard deviation (SD). (b) Spatial difference in CO_2 flux between the decoupled feedback case and the fully coupled POP2–waves simulation (decoupled minus POP2–waves). Shading denotes the mean difference, and overlaid contours indicate regions where the difference is statistically significant at the 95% confidence level based on a Student's t-test.

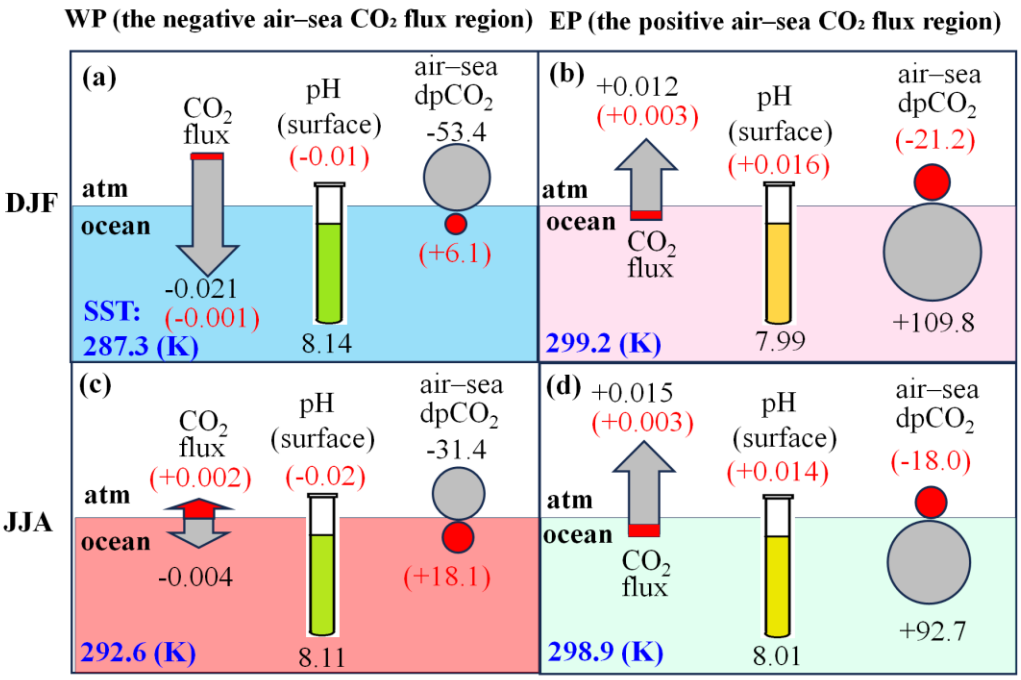

1473

1474 **Figure 11.** Schematic diagrams illustrate B–CTL (gray colors) and the differences
1475 between POP2–waves and B–CTL (red colors) in air–sea CO_2 flux (arrows), surface
1476 pH (tube colors indicator), and air–sea $dpCO_2$ (circle markers) over the oceanic CO_2
1477 uptake region (WP; 160–180°E, 35–40°N) and the oceanic CO_2 outgassing region
1478 (EP; 230–250°E, 0–5°S). Each panel includes an ocean-atmosphere interface, with
1479 ocean color shading representing relative SST levels across different seasons. The
1480 lower-left corner displays the SST value, (a) WP in DJF seasonal mean, (b) EP in DJF
1481 seasonal mean, (c) WP in JJA seasonal mean, and (d) EP in JJA seasonal mean.